2022-02

Global quasi-daily fractional vegetation cover estimated from the DSCOVR EPIC directio...

Version	Published version
Citation (published version):	W. Song, X. Mu, T.R. McVicar, Y. Knyazikhin, X. Liu, L. Wang, Z. Niu, G. Yan. 2022. "Global quasi-daily fractional vegetation cover estimated from the DSCOVR EPIC directional hotspot dataset." Remote Sensing of Environment, Volume 269, pp. 112835 - 112835. https://doi.org/10.1016/j.rse.2021.112835

https://hdl.handle.net/2144/44845
Boston University

Global quasi-daily fractional vegetation cover estimated from the DSCOVR EPIC directional hotspot dataset

Wanjuan Song [a,b,d], Xihan Mu [a,b,c,*], Tim R. McVicar [c], Yuri Knyazikhin [d], Xinli Liu [a,b], Li Wang [a], Zheng Niu [a,e], Guangjian Yan [a,b]

[a] *State Key Laboratory of Remote Sensing Science, Aerospace Information Research Institute-Chinese Academy of Sciences and Beijing Normal University, Beijing 100101&100875, China*
[b] *Beijing Engineering Research Center for Global Land Remote Sensing Products, Institute of Remote Sensing Science and Engineering, Faculty of Geographical Science, Beijing Normal University, Beijing 100875, China*
[c] *CSIRO Land and Water, GPO Box 1700, Canberra, ACT 2601, Australia*
[d] *Department of Earth and Environment, Boston University, Boston, MA 02215, USA*
[e] *University of Chinese Academy of Sciences, Beijing 100094, China*

ARTICLE INFO

ABSTRACT

Fractional Vegetation Cover (FVC) represents the planar fraction of the land-surface covered by green foliage, and its dynamics are important for an enhanced understanding of ecosystems especially how they respond to climate change. The lack of global near-real-time satellite-based products restricts the application of FVC in ecosystem modeling, climate change, and vegetation phenology studies. Earth Polychromatic Imaging Camera (EPIC) onboard Deep Space Climate Observatory (DSCOVR) spacecraft provides daily spectral reflectance of the entire sunlit Earth in the near Hotspot directions. Hotspot observations (i.e., observation in Hotspot direction which has the peak backscattering reflected radiation) with only sunlit vegetation and sunlit soil components are more suitable for FVC estimation with a two-endmember mixture model as such observations exclude contributions from shaded vegetation and soil components. In this study, an algorithm for retrieving quasi-daily FVC from EPIC based on two-endmember mixture and gap fraction models is developed. Analyses of its performance predict that the average Root-Mean-Square Deviations (RMSDs) of retrievals in FVC units is below 0.050 when compared with reference values. The RMSD is 0.043 when compared to field-based Landsat reference FVC, which confirms lower retrieval uncertainty than FVC retrieved from Low-Earth-Orbit (LEO) satellite products such as MODIS, VIIRS, and GEOV2 with RMSDs 0.049– 0.087. The comparison analyses suggest a good consistency between EPIC FVC and FVC products from LEO and geostationary (GEO) satellites sensor, SEVIRI, with RMSD values less than 0.129. EPIC allows for quasi-daily FVC estimation across the global terrestrial surface at 10 km resolution, which is an important development for numerous biophysical applications.

1. Introduction

Biophysical variables such as Fractional Vegetation Cover (FVC), defined as the planar fraction of the land-surface covered by photosynthetically active foliage (Carlson and Sanchez-Azofeifa, 1999; Deardorff, 1978; Lu et al., 2003; Ormsby et al., 1987; Sellers et al., 1996), are used to monitor vegetation dynamics. Accurate long-term high-frequency (even near-real-time) monitoring of FVC at large scales is important to climate change, ecosystem models, vegetation phenology, and other related terrestrial studies (Crowther et al., 2015; Hansen et al.,

2013; Hirano et al., 2004; Richardson et al., 2013). Models related to the land-surface and climate usually require near-real-time datasets, and with regional or global coverage (CTOS, 2010; García-Haro et al., 2019). Foley et al. (1996) demonstrated that neglecting FVC dynamics could cause substantial biases in climate change simulations. Accurately monitoring vegetation phenology depends primarily on the temporal frequency of satellite products (Ahl et al., 2006; Houborg and McCabe, 2018). Since rapid "green-up" may occur within 10 to 12 days for deciduous broadleaf forests (DBF; Ahl et al., 2006) and the temporal trend of the start/end of the growing season generally ranged from 0.2–8.2

days per year (Jeong et al., 2011; Liu and Zhang, 2020; Zhang et al., 2007) means using an 8- or 16-day composite product introduces errors when estimating the spring phenology signal (Ahl et al., 2006). Geostationary (GEO) satellites enable more frequent monitoring of vegetation phenology when compared to Low-Earth-Orbit (LEO) satellites (Sobrino et al., 2013; Yan et al., 2016a), yet such GEO products only cover specific regions. Therefore, globally consistent high-frequency (e. g., quasi-daily) FVC estimation will benefit global climate-earth system models and terrestrial land-surface studies.

Most global FVC products use LEO satellite remote sensing data at weekly to yearly temporal frequencies. Composite vegetation products from the Advanced Very High Resolution Radiometer (AVHRR), the Moderate-resolution Imaging Spectroradiometer (MODIS), the Visible Infrared Imaging Radiometer (VIIRS), and the Project for On-Board Autonomy-Vegetation (PROBA-V; product name: bioGEOphysical Vegetation product, GEOV) have temporal frequencies of 7 to 30 days (Baret et al., 2013; Ding and Zhu, 2018; Gutman and Ignatov, 1998; Jia et al., 2015; Myneni et al., 2015). Some regional FVC products, such as the GEO satellite Land Surface Analysis (LSA) FVC, have daily temporal frequencies (García-Haro et al., 2019). A global FVC product at a high temporal frequency ($<$ 8 days) is still unavailable.

Among FVC-estimation approaches for global production, the two-endmember linear mixture model (Eq. (1)) is one of the simplest, which scales Vegetation Index (VI) of pure vegetation (V_v) and bare soil (V_s) (Gutman and Ignatov, 1998; Jiapaer et al., 2011; Mu et al., 2018), as:

$$FVC = \frac{V - V_s}{V_v - V_s} \qquad (1)$$

V refers to any vegetation indices such as the Difference Vegetation Index (DVI), Normalized Difference Vegetation Index (NDVI), Enhanced Vegetation Index (EVI), etc. Both V_v and V_s are VI values in ideal situations. V_v is the VI value when vegetation fully covered the pixel area, which is hard to obtain via direct observation in arid and semi-arid areas. While it is a challenge to directly observe V_s in some forests. However, the mixture model is very sensitive to the values of V_v and V_s (Donohue et al., 2014; Montandon and Small, 2008; Mu et al., 2021; Yan et al., 2021). Mu et al. (2018) improved the VI-based model by developing a Multi-angle VI method (MultiVI) to estimate V_v, V_s, and FVC. The MultiVI is easy to implement and is as accurate as other physical models and machine learning methods in FVC estimation (Jia et al., 2015; Mu et al., 2018; Xiao et al., 2016). Additionally, numerous researchers improved this mixture model by adding more endmembers (Zhang et al., 2019; Gao et al., 2020; Defries et al., 1999; Guan et al., 2012).

In 2015, the Earth Polychromatic Imaging Camera (EPIC) onboard Deep Space Climate ObserVatoRy (DSCOVR) was launched to the Sun-Earth Lagrangian (L1) point. EPIC measures reflected sunlight in near-backscattering directions with the scattering angle between 168.5° and 175.5° (Marshak et al., 2018; Wen et al., 2019). The spectral reflectivity of the vegetated surface exhibits a sharp increase when the scattering direction approaches the direction of the Sun, which is known as the Hotspot effect in optical remote sensing (Kuusk, 1991; Nilson, 1991; Qin et al., 1996). EPIC provides images of the entire sunlit globe every 65– 110 min in 10 narrow spectral bands ranging from the ultraviolet to visible (4 bands) and near-infrared (NIR; 2 bands) at spatial resolutions of 10 km, resulting in multiple observations of each Earth's pixel in backscattering directions under different Solar Zenith Angles (SZAs). The daily maximum number of images available for the entire sunlit Earth's surface ranges from 13 (24 h × 60 min/h / 110 min) to 23 (24 h × 60 min/h / 65 min) following the winter-summer Earth-Sun illumination cycle. This provides a daily multi-SZA Hotspot dataset.

The Hotspot effect depends on both the reflective property of leaves and background as well as the illumination and observation geometry and spatial distributions of vegetation elements within the field of view of the sensor and therefore has potential for diagnosing canopy geometric structure (Hapke et al., 1996; Kuusk, 1991; Qin and Xiang, 1994; Qin et al., 1996). Studies have proved that the observations in near Hotspot direction is highly correlated with vegetation structure parameters (Cerstl and Simmer, 1986; Jupp and Strahler, 1991; Kuusk, 1985; Myneni and Kanemasu, 1988; Pisek et al., 2021; Qin and Xiang, 1994; Verstraete et al., 1990; Yang et al., 2017) and are critical for monitoring phenological changes in dense vegetation such as equatorial forests (Gorkavyi et al., 2021; Ni et al., 2021; Sun et al., 2021). Shadows that occurred in non-Hotspot observations had different amounts of impact on the VIs, with all indices significantly differing between the shaded and sunlit areas. These differences have proved to affect vegetation estimation (Barnes et al., 2015; Jiang et al., 2019; Zhang et al., 2015). Observations in the Hotspot direction, therefore, minimize the shadow impact (Hapke et al., 1996; Kuusk, 1991) and will allow for better FVC estimation.

To obtain global high-frequency (i.e., quasi-daily herein) FVC by using the near Hotspot daily observations from EPIC, our objectives are:

(i) developing a Multi-SZA HotSpot VI (MultiHSVI) based technique (which is primarily based on the MultiVI method) to estimate FVC;

(ii) assessing uncertainties by analyses of FVC retrieved from a simulated EPIC dataset, and comparison between FVC derived from EPIC and field measurements; and.

(iii) analyzing consistency between EPIC FVC and FVC from MODIS, VIIRS, GEOV, and LSA.

2. Data and materials

2.1. Hotspot dataset

Our primary dataset is the version 1 EPIC Level 2 (L2) Multi-Angle Implementation of Atmospheric Correction (MAIAC) product (10 km; 65– 110 min; Lyapustin et al., 2021), which is atmospherically corrected spectral Bidirectional Reflectance Factor (BRF) in the near Hotspot directions (https://asdc.larc.nasa.gov/project/DSCOVR/DSCOVR_EPIC_L2_MAIAC_01; last accessed 12/November/2021). The original EPIC image is 2048 × 2048 pixels. All bands (except for the band centered on 443 nm) have been downscaled and resampled to 1024 × 1024 pixels via a 2 × 2 moving window (Herman et al., 2018; Lyapustin et al., 2021; Marshak et al., 2018). By considering the effect of the optical point-spread function, the EPIC L2 product has a unified resolution of 10 km. Since the effective resolution decreases as the secant of the angle between EPIC's sub-Earth point and the normal to the Earth's surface, the effective resolution doubles at a viewing angle of 60° (20 km; Marshak et al., 2018). This resampling step alleviates the difference of the observed areas from different angles to a certain extent (Widlowski et al., 2008; Widlowski et al., 2006). EPIC MAIAC surface BRF is produced using the normalized 10 km resolution images (Lyapustin et al., 2021). The geometric positional accuracy has been verified by assessing the width of major rivers in Brazil and Egypt (Herman et al., 2018; Marshak et al., 2018). The radiometric resolution of EPIC data is 12 bits per pixel, which is the same as MODIS (Geogdzhayev and Marshak, 2018). The radiometric calibration has been investigated between EPIC, MODIS, and VIIRS, and was shown to agree within 5% (Geogdzhayev and Marshak, 2018 their Table 2; Yu and Wu, 2016 their Table 3).

Fig. 1 shows the daily numbers of global cloud-free observations per terrestrial pixel in EPIC L2 MAIAC images for 2016 according to the Day Of Year (DOY) and latitude, respectively. Here we used the SZA to group the cloud-free BRF. The threshold of 55° was used to determine the number of usable cloud-free BRF in a day as for SZA larger than this the reflectance values are usually unstable (Marshak, 2020; Marshak and Ward, 2018). On average there were up to 6 cloud-free daily BRF values per pixel during winter in 2016 which increased to 10 during summer (Fig. 1(a)). According to Fig. 1(b), cloud-free BRF with small SZA (i.e., SZA $<$ 45°) appears between 65° north latitude (65°N) and 65° south
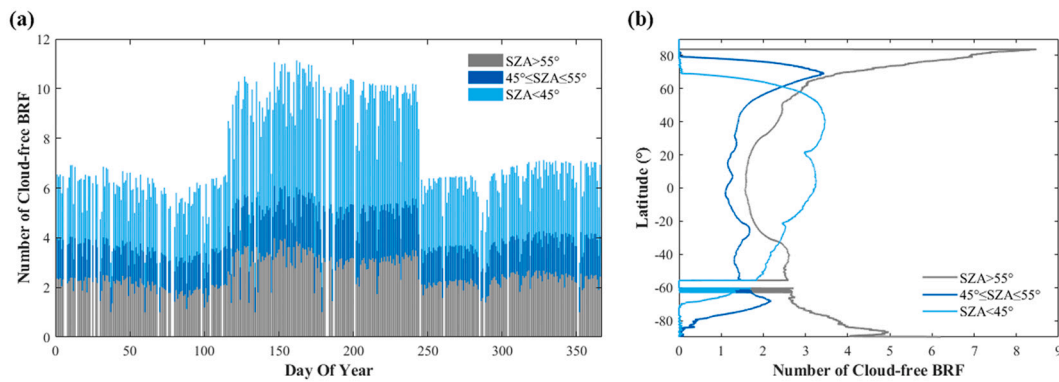
Fig. 1. The number of daily cloud-free land-surface BRFs in EPIC images per terrestrial pixel for 2016. Part (a) shows the global average numbers according to Day Of Year, and (b) presents the averaged numbers according to latitude, where the positive value means north latitude and the negative value means south latitude. Numbers are broken down into BRF with the SZA (i) above 55° (grey); (ii) between 45° and 55° (dark blue); and (iii) below 45° (light blue). (For interpretation of the references to colour in this figure legend, the reader is referred to the web version of this article.)

latitude (65°S), and usable cloud-free BRF appears (i.e., SZA ≤ 55°) between 77°N and 77°S. The ocean pixels are removed in Fig. 1, which is why there is no cloud-free BRF near 60°S in Fig. 1(b).

The surface BRF product (Lyapustin et al., 2021) are available at 6 of the 10 narrow spectral bands centered at: (i) 340 nm (band-width (BW) 3.0 nm); (ii) 388 nm (BW 3.0 nm); (iii) 443 nm (BW 3.0 nm); (iv) 551 nm (BW 3.0 nm); (v) 680 nm (BW 2.0 nm); and (vi) 779.5 nm (BW 2.0 nm). EPIC began measurements in June 2015. We use BRF data in the red (680 nm) and NIR (779.5 nm) bands in 2016 (i.e., the first complete calendar year of EPIC data).

2.2. Simulated EPIC dataset

The three-dimensional (3D) radiative transfer (RT) simulation framework, LESS (large-scale remote sensing data and image simulation framework over heterogeneous 3D scenes; http://lessrt.org/; last accessed 12/November/2021), was used to generate a simulated dataset. Qi et al. (2019) showed that LESS is faster and has similar or even better accuracy than other 3D RT models. Herein, both Hotspot reflectance in red (680 nm) and NIR (779.5 nm) bands as well as Red-Green-Blue (RGB) orthogonal projection images for three scenes (100 m × 100 m) were simulated. The three scenes are: (i) homogeneous scene (HOM; Fig. S1 (a) and Table S1); (ii) heterogeneous scene with spherical crowns (HET1; Fig. S1 (b) and Table S1); and (iii) heterogeneous scene with spherical and cylinder-shaped crowns (HET2; Fig. S1 (c) and Table S1). Nine Leaf Area Index (LAI) levels (i.e., 0.5, 1.0, 1.5, 2.0, 3.0, 4.0, 5.0, 5.5 and 6.0) were used to represent a range of vegetation coverage conditions. Uniform and spherical Leaf Angle Distributions (LADs) were simulated. The two groups of soil reflectance were selected to represent dark and bright underground; Soil 1 and 2 in Table S2 represent high and low soil reflectivity, respectively. Full details are provided in Supplementary Material (Sec. S1).

2.3. Reference dataset

Field measurements of FVC were made at 26 plots for the primary vegetation types at Saihanba, in northern China (Fig. 2; Table S4) using digital camera photography (Mu et al., 2015). The plot size was 45 m × 45 m to represent a Landsat pixel. The digital images were processed to obtain field-measured FVC by using an automatic and shadow-resistant algorithm (SHAR-LABFVC) with an uncertainty of less than 0.025 (Song et al., 2015).

Landsat 8 Operational Land Imager (OLI) atmospherically corrected surface reflectance data (30 m; 16 days; https://www.usgs.gov/land-resources/nli/landsat/; last accessed 12/November/2021; Vermote et al., 2016) was obtained to generate reference FVC for validation
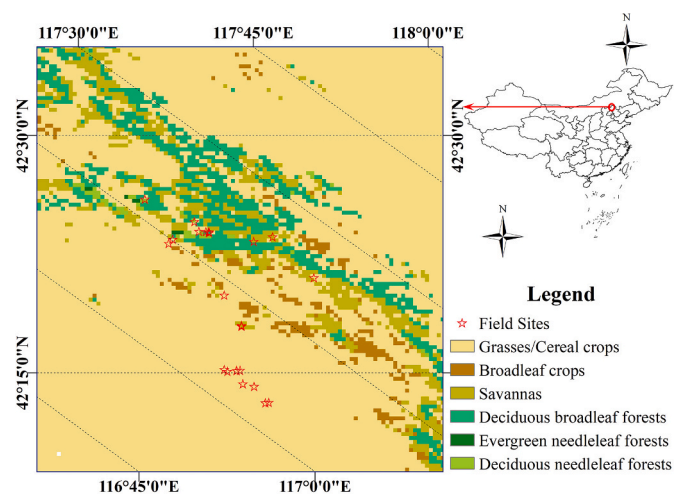

Fig. 2. Land cover types in the Saihanba area (50 km × 60 km) from 500 m MODIS land cover type product (MCD12Q1 from Collection 6) in 2016. Land cover type 3 for the MODIS-derived Leaf Area Index (LAI) and Fraction of Photosynthetically Active Radiation (FPAR) scheme (Friedl et al., 2010) is used herein. Red stars locate the 26 FVC field-sites. (For interpretation of the references to colour in this figure legend, the reader is referred to the web version of this article.)

in 10 km spatial resolution, following a generic four-step up-scaling approach (McVicar et al., 1996a; McVicar et al., 1996b; Mu et al., 2015). Firstly, NDVI was calculated based on the Landsat surface reflectance. Secondly, an empirical transfer function (Eq. (2) was used herein) was established to convert NDVI into FVC. In Eq. (2), *a*, *b*, and *k* are conversion coefficients that are dependent on land type and growth date. We obtained the conversion coefficients using the field-measured FVC at 26 vegetation plots and a desert plot (a plot with very low vegetation coverage; Table S4) as well as the Landsat NDVI spatially and temporally close to the field measurements. Thirdly, Eq. (2) was applied to the whole Landsat NDVI images at the Saihanba area in 2016 to estimate the 30 m field-based Landsat FVC images. Fourthly, the 30 m FVC located in the same 10 km EPIC pixel area were arithmetically averaged to obtain the 10 km field-based Landsat reference FVC (Fig. 3).

$$\text{FVC} = (a \bullet NDVI + b)^k \tag{2}$$

2.4. Similar satellite-based products

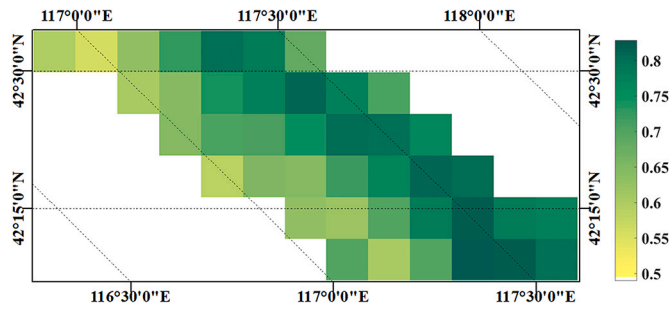To analyze the utility of our method, four other satellite vegetation

Fig. 3. Field-based Landsat reference FVC at 10 km spatial resolution in the Saihanba area on 31 July 2016. The white colour in this image represents non-estimated value. The data are shown in the same sinusoidal projection as the EPIC data. The average standard deviation of 30 m field-based Landsat reference FVC in each 10 km resolution EPIC pixel is 0.126.

products (Table 1) were compared, being: (i) MODIS LAI suite (MCD15A2H; Myneni et al., 2015) and MODIS Clumping Index (CI) data (He et al., 2012); (ii) VIIRS Green Vegetation Fraction (GVF; Ding and Zhu, 2018; Vargas et al., 2013); (iii) second version of GEOV (GEOV2) FVC from PROBA-V (Verger et al., 2014ab); and (iv) LSA FVC from Spinning Enhanced Visible and Infrared Imager (SEVIRI) onboard the GEO Meteosat Second Generation (MSG) platform (García-Haro et al., 2019).

We chose three 10° by 10° regions as study areas. The Mississippi region (centered on 35°0′E, 91°4′W) in the southern USA was selected as it exhibited a rich diversity of vegetation types (Fig. 4) having a good-quality EPIC data in 2016. Study regions (Fig. 5) in central Africa (centered on 5°0′N, 25°0′E) and southern Africa (centered on 25°0′S, 27°34′E) were located in the center of SEVIRI coverage provided different vegetation types (i.e., shrubs and evergreen broadleaf forests (EBF)) to those found in the Mississippi region (i.e., grass/cereal crops, broadleaf crops, savannas, and DBF).

3. Theory and methodology

3.1. Hotspot observations

The signal received by the satellite sensor can be modeled as a composite of reflected light from vegetation, background, and their shadows within the field of view. Thus, it can be presented as a linear combination of four components and their areal proportions (Li and Strahler, 1985; Li and Strahler, 1992; Strahler and Jupp, 1990; Woodcock et al., 1997).
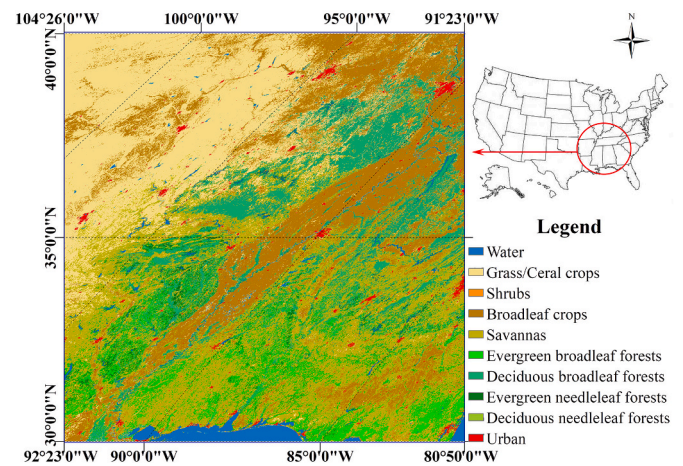

Fig. 4. Land cover map from MODIS (MCD12Q1) for 2016 over the 10° by 10° Mississippi region.

$$S = K_C C + K_g G + K_t T + K_z Z \qquad (3)$$

In Eq. (3), S is the signal of a pixel, K_c, K_g, K_t, and K_z represent the areal proportions of sunlit vegetation, sunlit background, shaded vegetation, and shaded background with C, G, T, and Z being the spectral signatures of the respective components. However, in Hotspot observations, there is no shaded vegetation and shaded background in the field of view. Thus, Eq. (3) can be simplified as the combination of the remaining two components.

$$S = K_C C + K_g G \qquad (4)$$

The VI-based two-endmember mixture model is commonly used in FVC estimation (Donohue et al., 2014; Ding and Zhu, 2018; Gao et al., 2020; Gutman and Ignatov, 1998; Zeng et al., 2000). It assumes that a pixel is a mixture of only vegetation and background (Gutman and Ignatov, 1998), yet the VI values are considerably influenced by shadows (Barnes et al., 2015; Jiang et al., 2019; Zhang et al., 2015). Noting that shadows appear relatively darker in red band images than NIR band images as vegetation generally absorbs red light and scatters NIR light (Barnes et al., 2015; Jiang et al., 2019; Zhang et al., 2015). Therefore, using the Hotspot observations is expected to improve the accuracy of FVC estimation using the two-endmember mixture model.

Table 1

Satellite-based vegetation products used to compare with EPIC FVC. All data links were last accessed on 12/November/2021.

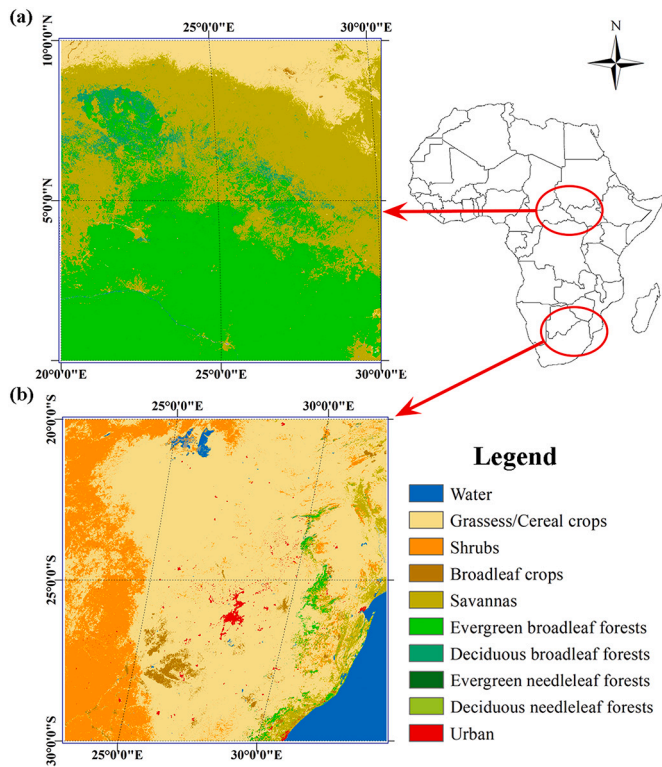| Project/ Satellite sensor	Product	Resolution	Algorithm (FVC estimation; Noise reduction)	Validation & Uncertainty	Reference	Data link
MODIS	1) MCD15A2H (LAI) 2) CI	1) 500 m; 8 days 2) 500 m; 1 year	Gap fraction model; 8-day composition	1) RMSD = 0.6; bias = ±1 2) R² = 0.76	Myneni et al., 2015 He et al., 2012	https://modis.gsfc.nasa.gov/data/dataprod/mod15.php https://daac.ornl.gov/VEGETATION/guides/Global_Clumping_Index.html
VIIRS	Green Vegetation Fraction (GVF)	4 km; 1 day	VI-based two-endmember linear mixture model; A daily rolling 15-week Gorry filter	RMSD = 0.116	Ding and Zhu, 2018	https://viirsland.gsfc.nasa.gov/Products/NOAA/GVF.html
GEOV2	FVC	≈1 km; 10 days	Neural network method; 2– 4 months' Savitzky-Golay filter	RMSD = 0.14	Verger et al. 2014a; Verger et al., 2014b	https://land.copernicus.eu/global/products/fcover
LSA	FVC	3.1 km; 1 day	Stochastic spectral mixture model; A recursive scheme using a 20-day composite window	RMSD = 0.17	García-Haro et al., 2019	https://navigator.eumetsat.int/product/EO:EUM:DAT:MSG:FVC-SEVIRI?query=&filter=satellite_MSG&filter=themes_Land&results=40&s=extended

(a)

(b)

Legend
- Water
- Grassess/Cereal crops
- Shrubs
- Broadleaf crops
- Savannas
- Evergreen broadleaf forests
- Deciduous broadleaf forests
- Evergreen needleleaf forests
- Deciduous needleleaf forests
- Urban

Fig. 5. Land cover maps from MCD12Q1 for 2016 over (a) central Africa and (b) southern Africa regions.

3.2. MultiHSVI FVC estimation method

MultiHSVI, developed herein, takes advantage of Hotspot observations to better estimate FVC. It is developed for estimating V_v and V_s values, which in turn, are used to estimate FVC based on the VI-based two-endmember mixture model (Eq. (1)). Herein, we use the two-band EVI (EVI2; Jiang et al., 2008) as an example for FVC estimation, as it has a stronger correlation with vegetation biophysical parameters (e.g., FVC, LAI) than NDVI (Houborg et al., 2007; Morcillo-Pallarés et al.,

2019; Xiao et al., 2004) and avoids the uncertainty of using the blue band to calculate EVI (Huete, 1988).

MultiHSVI produced global quasi-daily FVC using the Hotspot dataset from EPIC in two steps: (i) retrieving V_v and V_s of EVI2 and (ii) FVC estimation. Fig. 6 is the flowchart to estimate EPIC FVC by MultiHSVI.

3.2.1. Retrieving V_v and V_s of EVI2

The V_v and V_s retrieval procedure combines the EVI2-based two-endmember non-linear mixture model (Choudhury et al., 1994; Gitelson, 2004, 2013; Gitelson et al., 2002)

$$f(\theta) = \left(\frac{V(\theta) - V_s}{V_v - V_s}\right)^n \qquad (5)$$

and the gap fraction model (Nilson, 1971)

$$p(\theta) = e^{-G(\theta) \cdot \Omega(\theta) \cdot LAI/cos\theta} \qquad (6)$$

Here $f(\theta)$ is the directional vegetation cover, which describes the vegetation coverage at View Zenith Angle (VZA) θ. $f(\theta)$ and FVC are identical when θ equals zero. $V(\theta)$ denotes EVI2 for VZA as θ. n is the nonlinearity coefficient, which is used to fit the slight nonlinear $V(\theta)$ and $f(\theta)$ relationship. This nonlinear relationship usually appears in very dense vegetation when multiple scattering effects are substantial and the saturation problem occurs (Choudhury et al., 1994; Gitelson, 2004, 2013; Gitelson et al., 2002). G is the geometry factor that is related to LAD (Goel and Strebel, 1984; Wang et al., 2007). The directional vegetation cover $f(\theta)$ equals "$1 - p(\theta)$". Therefore, Eqs. (5) and (6) can be combined as

$$1 - \left(\frac{V(\theta) - V_s}{V_v - V_s}\right)^n = e^{-G(\theta) \cdot \Omega(\theta) \cdot LAI/cos\theta} \qquad (7)$$

Then, the EVI2 in different VZAs is used to estimate V_v, V_s, and n. EVI2 ($V(\theta_1)$, $V(\theta_2)$, $V(\theta_3)$, ..., $V(\theta_i)$, $V(\theta_j)$, ..., $V(\theta_x)$) at a pixel is sorted according to VZA ($\theta_1 < \theta_2 < \theta_3 ...... < \theta_i < \theta_j ......\theta_x$). Every two adjacent sets of observations (both angularly and temporally) are grouped as a pair. Eq. (7) can be reorganized with a pair of observations (denoted as θ_i and θ_j herein) as:

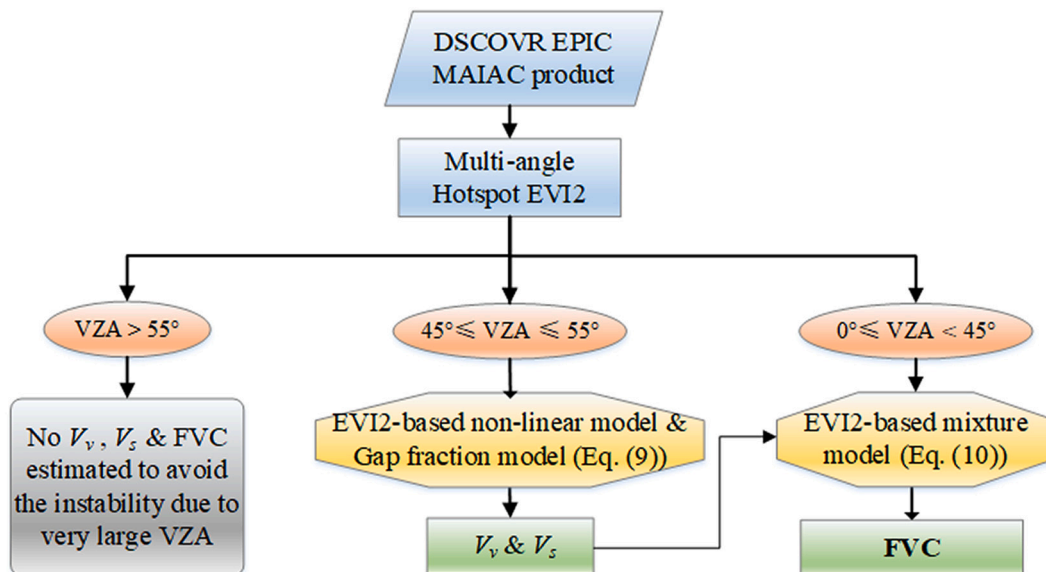$G(\theta)$ and $\Omega(\theta)$ in Eq. (8) are often assumed as constant for satellite-

Fig. 6. Processing flowchart to generate EPIC FVC, with VZA denoting the View Zenith Angle. V_v and V_s denote the EVI2 of fully-covered vegetation and bare soil, respectively.

$$\begin{cases} \left(1 - \left(\dfrac{V(\theta_i) - V_s}{V_v - V_s}\right)^n\right)^{cos\theta_i} = e^{-G(\theta_i)\bullet\Omega(\theta_i)\bullet LAI} \left(1 - \left(\dfrac{V(\theta_j) - V_s}{V_v - V_s}\right)^n\right)^{cos\theta_j} = e^{-G(\theta_j)\bullet\Omega(\theta_j)\bullet LAI} \end{cases} \qquad (8)$$

based vegetation studies (Chen et al., 1999; He et al., 2012; Mu et al., 2018; Roujean et al., 1992; Song et al., 2017; Wanner et al., 1995), especially for VZA around 57.5° (Mu et al., 2018; Weiss et al., 2004). Moreover, the angular variation of $cos\theta$ is relatively larger than the angular variation of $G(\theta)\bullet\Omega(\theta)$ at large VZA (Section 5.1 and S3). Therefore, $G(\theta)\bullet\Omega(\theta)$ can be assumed as an unknown constant when estimating V_v, V_s, and n with observations at VZA larger than 45° herein (Fig. 6). This means that $e^{-G(\theta_i)\bullet\Omega(\theta_i)\bullet LAI}$ approximates $e^{-G(\theta_j)\bullet\Omega(\theta_j)\bullet LAI}$. Eq. (8) can be rewritten as below:

$$\left(1 - \left(\dfrac{V(\theta_i) - V_s}{V_v - V_s}\right)^n\right)^{cos\theta_i} = \left(1 - \left(\dfrac{V(\theta_j) - V_s}{V_v - V_s}\right)^n\right)^{cos\theta_j} \qquad (9)$$

Eq. (9) only relates to $V(\theta)$ and parameters V_v, V_s, and n for a single pixel. V_v, V_s, and n can be obtained with at least three pairs of angular observations.

3.2.2. FVC estimation

The FVC estimation procedure is based on the EVI2-based two-endmember mixture model (Eq. (1)). In Eq. (1), V_v and V_s have been estimated in Section 3.2.1, and the VI of the pixel should be the EVI2 at a VZA of zero. Herein, EVI2 with small VZA (i.e., VZA < 45°) at each pixel are arithmetically averaged and used for the estimation of FVC as only a few pixels were observed at nadir for the EPIC sensor. Then, FVC can be calculated as Eq. (10)

$$FVC = \frac{\overline{V(\theta_{small})} - V_s}{V_v - V_s} \qquad (10)$$

where, $\overline{V(\theta_{small})}$ is the averaged EVI2 with small VZA (θ_{small}). The uncertainty of zenith angle variation in FVC estimation is discussed in Sec. 5.2.3.

3.3. Implementation based on EPIC data

MultiHSVI was applied to the EPIC MAIAC surface multi-SZA Hotspot BRF product. In this product, VZA is close to SZA as the EPIC sensor observes the Earth essentially in the Hotspot direction. Thus, the SZA from EPIC MAIAC BRF product was used for V_v, V_s, and FVC production herein.

During V_v and V_s production, Hotspot EVI2 over all 2016 was used to provide sufficient observations, as these two parameters are mainly determined by vegetation type and soil type, respectively (Ding et al., 2016 their Fig. 4; Montandon and Small, 2008 their Table 1; Zeng et al., 2000 their Table 1). To provide parsimonious model parameterization, which was based primarily on EPIC data, other influences such as intra-year vegetation changes (e.g., crops) and soil moisture changes were not considered. The abnormal Hotspot EVI2 values (e.g., ≤ 0.01) were excluded, which means observations influenced by snow, ice, water, and other noises are excluded. Hotspot EVI2 with an SZA greater than 55° was also removed to avoid the instability due to very large SZA (Marshak, 2020; Marshak and Ward, 2018). The boundary values of V_v and V_s were optimized based on the statistics of EVI2 from EPIC and global soil spectral libraries (Clark et al., 1992; Garrity and Bindraban, 2004).

To avoid the error caused by the non-uniform distribution of SZA, we added a four-step equation selection procedure for retrieving V_v and V_s. Firstly, all the Hotspot EVI2 pairs for each pixel mentioned in Section 3.2.1 are sorted based on their maximum values (i.e., according to the larger EVI2 value in each pair). Secondly, the EVI2 pairs were divided into groups of large EVI2 and low EVI2. Thirdly, four pairs of EVI2 uniformly distributed (i.e., at the top of each quartile of the accumulative histogram) in each group were selected to estimate V_v and V_s based on Eq. (9). Fourthly, V_v estimated from the group of larger EVI2 values was set as the V_v at this pixel (as higher EVI2 values are closer to V_v) and V_s estimated from the group of lower Hotspot EVI2 values was set as the V_s at this pixel (as lower EVI2 values are closer to V_s).

FVC was estimated for the pixels that have at least one cloud-free BRF (the number of globally averaged daily cloud-free BRF is provided in Fig. 1). FVC estimates beyond the physically plausible 0 to 1 range were set to 0 and 1 (as appropriate) during production. A corresponding quality file recorded which estimates were beyond the physically plausible range and which estimates were from observations with large SZA ($45° \leq SZA \leq 55°$; Fig. 6 and dark blue in Fig. 1).

4. Evaluation results

4.1. FVC results analysis using simulated EPIC dataset

Fig. 7 presents the evaluation of MultiHSVI using data simulated in Section 2.2 and Sec. S1. Each data point represents the FVC obtained from one scene. We implemented the newly developed MultiHSVI, the original MultiVI, and the traditional gap fraction model method, respectively. Here, the Normalized Difference between Hotspot and Darkspot (NDHD) index calculated from the simulated dataset was used to estimate CI in the gap fraction model, which was used to characterize the heterogeneity of vegetation (Chen et al., 2005). LAI needed in the gap fraction model and the reference FVC (Table S3) were obtained from the simulated scenes. EVI2 with LAI values from 0.5 to 6.0 representing a range of vegetation conditions (i.e., FVC: 0.1–1.0) were simulated.

According to Fig. 7(a), FVC estimated by MultiHSVI has lower uncertainty than the original MultiVI and the traditional gap fraction model method. In these simulated scenes, the R^2 between MultiHSVI FVC and the reference as well as MultiVI FVC and the reference are all greater than 0.970, while the R^2 between gap fraction model retrieved FVC and the reference is 0.877. The p-value in the significance t-test with a confidence level equal to 90% is less than 0.001. Meanwhile, the FVC estimated by MultiHSVI and MultiVI have less uncertainty (i.e., a smaller RMSD) than the FVC estimated by the gap fraction model. The RMSDs for MultiHSVI and MultiVI are 0.046 and 0.070, respectively, while for the gap fraction model, it is 0.125 (Fig. 7(a)). The error could come from LAI and/or CI.

Additionally, MultiHSVI has lower uncertainty than MultiVI and gap fraction model method under different vegetation conditions. Fig. 7(b) $\sim$ (d) show the FVC estimation comparison for a range of vegetation conditions. Sparse vegetation conditions (i.e., LAI = 0.5, 1.0, 1.5; FVC < 0.5 for most simulations) represents arid and semi-arid regions where vegetation coverage is always sparse. Medium vegetation conditions (i.e., LAI = 2.0, 3.0, 4.0; 0.3 < FVC < 0.8 for most simulations) represents the growing period of vegetation such as crops and deciduous forests. Dense vegetation conditions (i.e., LAI = 5.0, 5.5, 6.0; FVC > 0.7)
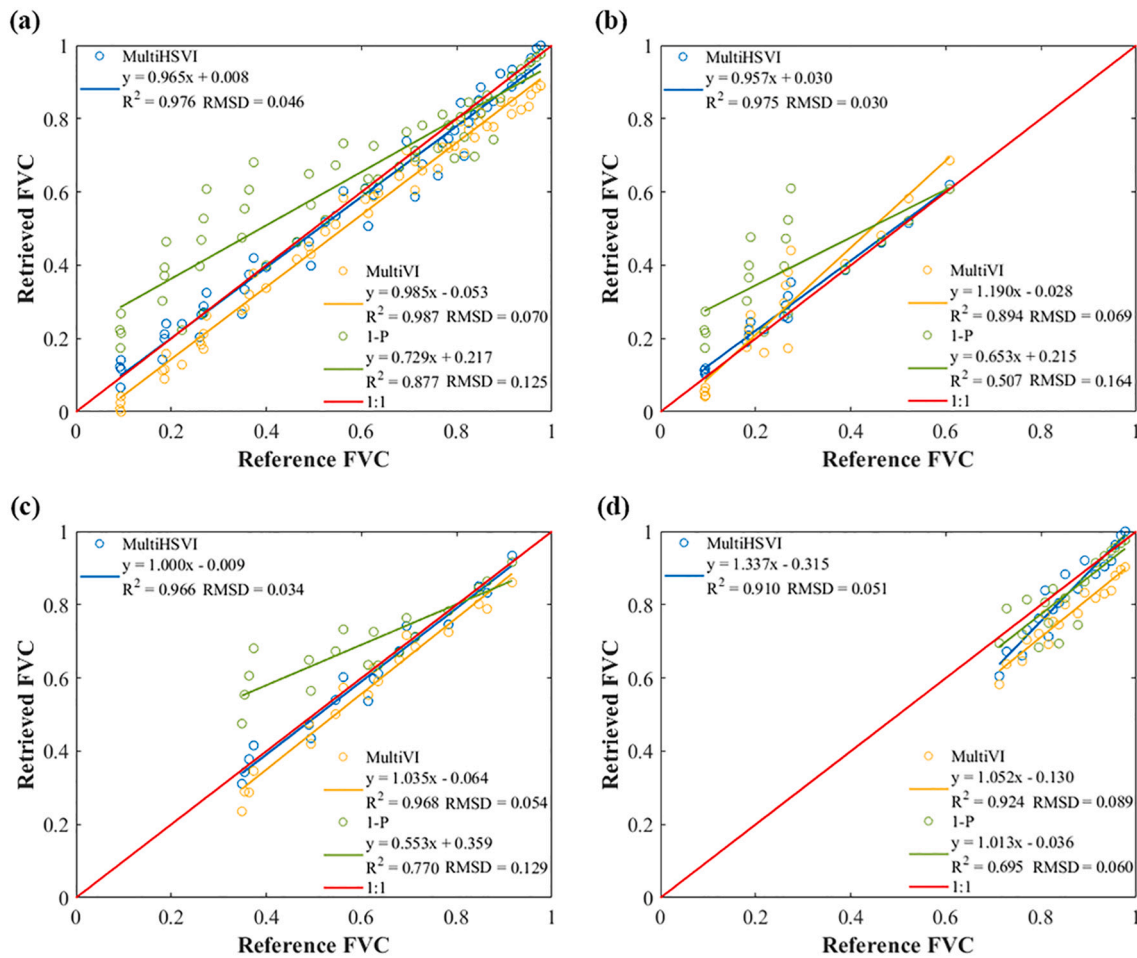
Fig. 7. Analysis of FVC estimation using simulated EPIC dataset based on the LESS model. Comparison of retrieved FVC versus the reference for (a) all vegetation conditions (i.e., LAI from 0.5 to 6.0), (b) sparse vegetation conditions (i.e., LAI = 0.5, 1.0, 1.5), (c) medium vegetation conditions (i.e., LAI = 2.0, 3.0, 4.0), and (d) dense vegetation conditions (i.e., LAI = 5.0, 5.5, 6.0).

represents areas such as the tropical humid region where vegetation is always dense. The RMSDs for MultiHSVI under sparse (0.030) and medium (0.034) vegetation conditions are all below 0.050. While the RMSD under dense vegetation conditions is 0.051 due to NIR band saturation, which highly affects EVI2. However, for MultiVI, there is a relatively large uncertainty (as quantified by RMSD) compared with MultiHSVI for all three vegetation conditions with RMSDs from 0.054 to 0.089 for MultiVI yet being only 0.030 to 0.051 for MultiHSVI (Fig. 7(b) ~ (d)). The gap fraction model method has lower uncertainty in dense vegetation conditions (RMSD = 0.060) than sparse (RMSD = 0.164) to medium (RMSD = 0.129) vegetation conditions. However, it has higher uncertainties than MultiHSVI over all three vegetation conditions. Therefore, we conclude that the MultiHSVI method is an improvement over the MultiVI method, as it introduced a lower uncertainty of around 0.050 in FVC units when analyzed with this simulated dataset. Additionally, both MultiHSVI and MultiVI methods are independent of vegetation structure parameters such as LAI and CI and yield lower uncertainty than the gap fraction model.

4.2. Comparison with the field-based Landsat FVC

Comparisons between EPIC FVC and FVC from MODIS, VIIRS, and GEOV2 products with the field-based Landsat reference FVC (Fig. 3) are shown in Fig. 8. The field-based Landsat FVC on 31 July 2016 was used as most field-measurements (Table S4) were implemented between 29 July and 3 August. The temporal information of EPIC, MODIS, VIIRS and GEOV2 is listed in Table 2.
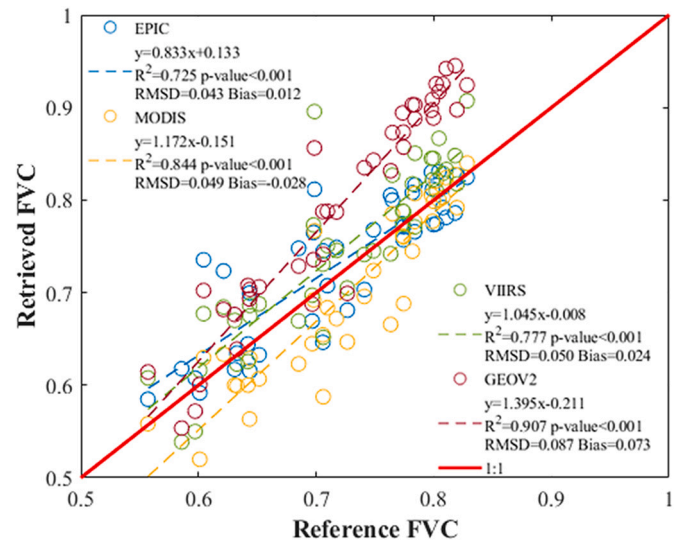

Fig. 8. Comparison of retrieved FVC from EPIC, MODIS, VIIRS, and GEOV2 with field-based Landsat reference FVC over the Saihanba area.

According to Fig. 8, EPIC FVC estimated by MultiHSVI has lower uncertainty than MODIS, VIIRS, and GEOV2 FVC (Table 1). EPIC FVC agrees well with the reference FVC with an R^2 of 0.725 (p-value

Table 2
Temporal information of the EPIC, MODIS, VIIRS, and GEOV2 FVC products during 2016.

Project / Satellite sensor	Target time	Temporal composition period
EPIC	31 July	23 July to 7 August
MODIS	31 July	27 July to 11 August
VIIRS	31 July	25 July to 6 August
GEOV2	31 July	1 June to 30 September

<0.001), an RMSD of 0.043, and a bias of 0.012. FVC from MODIS (RMSD = 0.049) and VIIRS (RMSD = 0.050) have the similar uncertainty and the biases are 0.028 and 0.024, respectively. Because VIIRS was designed to be "the successor" to MODIS, they are onboard similar satellites (having a similar observation mode concerning the timing of data acquisition and orbital parameters) and have similar spectral bands. The RMSD between GEOV2 FVC and the reference FVC is 0.087, which is worse than that reported for the other three FVC products in this comparison. However, GEOV2 FVC has greater correlation with the reference FVC with an R^2 of 0.907 (p-value <0.001). According to Fig. 8, GEOV2 overestimates FVC in dense vegetation areas (FVC > 0.7; bias = 0.073). This concords with Verger et al.'s (2014a) conclusion that GEOV2 FVC has a tendency to overestimate cropland measurements, mainly for medium to high FVC values (i.e., 0.3– 1.0). This overestimation is likely due to the fixed rescaling factor used in GEOV2 FVC production (Baret et al., 2013; Verger et al., 2014a). Thus, we concluded that MultiHSVI has advantages when applied to EPIC data. Note that the uncertainties in field-based Landsat reference FVC values will also affect these FVC comparison results.

4.3. Comparison of FVC from MODIS, VIIRS, GEOV2, and LSA

The comparisons between EPIC FVC and FVC from MODIS, VIIRS, GEOV2, and LSA were made in the Mississippi region (Fig. 4) and the two African regions (Fig. 5; noting that LSA data do not cover the Mississippi region). Detailed spatial and temporal information of each product is listed in Table 3.

4.3.1. Comparison of spatial pattern

The per-pixel comparisons of FVC from EPIC, MODIS, VIIRS, and GEOV2 were conducted over the Mississippi region (Fig. 9 and S2) which is more heterogeneous than the Saihanba area used in Section 4.2 and the central and southern Africa regions, where LSA FVC estimates were additionally used in the comparison (Figs. 10, S3, and S4). Here the central Africa and southern Africa regions in Fig. 5 were combined for statistics. According to Fig. 9(a) ~ (c) and 10(a) ~ (d), the differences (RMSD) between EPIC FVC and FVC from MODIS, VIIRS, GEOV2, and LSA are less than 0.129, which is consistent with the reported uncertainty of these products (Table 1). The overall correlation between EPIC FVC and the FVC from the other 4 products are over 0.758 (R^2); the correlations over the Africa regions are higher than Mississippi since its

Table 3
Spatial and temporal information of the FVC from EPIC, MODIS, VIIRS, GEOV2, and LSA during 2016.

Project /Satellite sensor	Spatial coverage	Target date	Temporal composite period
EPIC	Mississippi	10 June	1 to 16 June
	Africa	30 April	22 April to 9 May
MODIS	Mississippi	10 June	9 to 16 June
	Africa	30 April	30 April to 7 May
VIIRS	Mississippi	10 June	4 to 16 June
	Africa	30 April	24 April to 6 May
GEOV2	Mississippi	10 June	1 March to 30 June
	Africa	30 April	11 April to 10 August
LSA	Africa	30 April	Not mentioned by the producer

land cover is relatively homogenous. This means that EPIC FVC can capture the spatial variation of vegetation over a wide range of regions (Fig. 9(a) ~ (c) and 10(a) ~ (d)).

The differences among FVC from MODIS, VIIRS, GEOV2, and LSA are relatively higher. The overall correlation (R^2) and difference (RMSD) among EPIC, MODIS, VIIRS, GEOV2, and LSA are around 0.758– 0.951 and 0.066– 0.151, respectively (Figs. 9 and 10). These differences are influenced by both land cover type and the FVC estimation method. The difference between MODIS and VIIRS FVC over the Mississippi region (RMSD = 0.151) is the largest of all comparison results, while the RMSD is only 0.100 over the two African regions. Considering that MODIS and VIIRS FVC have the most consistency over Saihanba areas (Fig. 8), this difference could be explained by the land covers. LSA FVC has been reported to have a good consistency with GEOV1 FVC (Camacho et al., 2018) which is also consistent with GEOV2 FVC (Baret and Weiss, 2019). According to Fig. 10(j), the R^2 between GEOV2 and LSA is 0.945 with an RMSD of 0.079 and a bias of 0.037. The relative relations between EPIC FVC and FVC from GEOV2 and LSA are similar (Fig. 10(c) and (d)). The artificial truncation along the right-hand edge of the data cloud of MODIS (at 0.9 FVC) and LSA (at 0.97 FVC) in Fig. 10(a) and (d), respectively, is caused by saturation in the MODIS LAI and LSA FVC products. This artificial truncation issue is seen elsewhere (e.g., Fig. 11 (e) and Fig. S6(b)).

4.3.2. Comparison of land cover types

Since the uncertainty of FVC products can be land-cover-type-dependent, the performances of five FVC products for six major land cover types were analyzed, i.e., (i) grass/cereal crops (e.g., rice and wheat); (ii) shrubs; (iii) broadleaf crops (e.g., soybean and cotton); (iv) savannas; (v) EBF; and (vi) DBF. The land cover type information was derived from MCD12Q1 for 2016. Herein, the majority class of the 500 m resolution MODIS pixels contained in a 10 km EPIC pixel are used to define the class of each EPIC pixel. The per-pixel comparisons between EPIC and MODIS, and between EPIC and GEOV2 over different land cover types are shown in Figs. 11 and 12, with EPIC-VIIRS and EPIC-LSA provided in Figs. S5 and S6, respectively.

Fig. 11 shows that EPIC FVC is lower than MODIS FVC over broadleaf crops areas and agrees well with MODIS FVC over grass/cereal crops when MODIS LAI has good accuracy (Yan et al., 2016b their Table 3). As for the uncertainty of MODIS FVC from LAI and CI products, it is reported that MODIS LAI has good accuracy over grass/cereal crops areas (Yan et al., 2016b their Table 3) and usually underestimates both cereal and broadleaf crops LAI (Fang et al., 2019 their Fig. 11). According to Fig. 11(a), the difference (RMSD) between EPIC and MODIS FVC is 0.087 with a bias of 0.018 for grass/cereal crops, which is the smallest bias among all land cover types. However, EPIC FVC is higher than MODIS FVC over broadleaf crops areas (Fig. 11(c)). Therefore, EPIC FVC should have good accuracy over grass/cereal crops areas and lower uncertainty than MODIS FVC over broadleaf crops. The EBF areas have dense vegetation, and saturation problems are often encountered when using remote sensing to estimate LAI/FVC in this area.

According to Fig. 12(c), (e), and (f), EPIC FVC agrees well with GEOV2 FVC for the broadleaf crops but is lower than GEOV2 for EBF and DBF where GEOV2 usually overestimated FVC (Pérez et al., 2019 their Fig. 46 and Annex III; Verger et al., 2014a their Table 1 and Fig. 11). GEOV2 FVC has an uncertainty of around 0.1 over grass, crops, and forest areas (Camacho et al., 2013 their Fig. 19; Pérez et al., 2019 their Fig. 46 and Annex III). In addition, it has good accuracy for the crops, yet overestimates FVC for EBF and DBF with high FVC (Pérez et al., 2019; Verger et al., 2014a). Therefore, the difference between EPIC and GEOV2 FVC over grass/cereal crops (RMSD = 0.083, bias = 0.005) reveals that EPIC should have good accuracy over grass/cereal crops. The biases between EPIC and GEOV2 FVC over EBF (RMSD = 0.180, bias = −0.165) and DBF (RMSD = 0.089, bias = −0.029) are negative, meaning that the EPIC FVC estimate is lower than that from GEOV2 for these two land cover types.
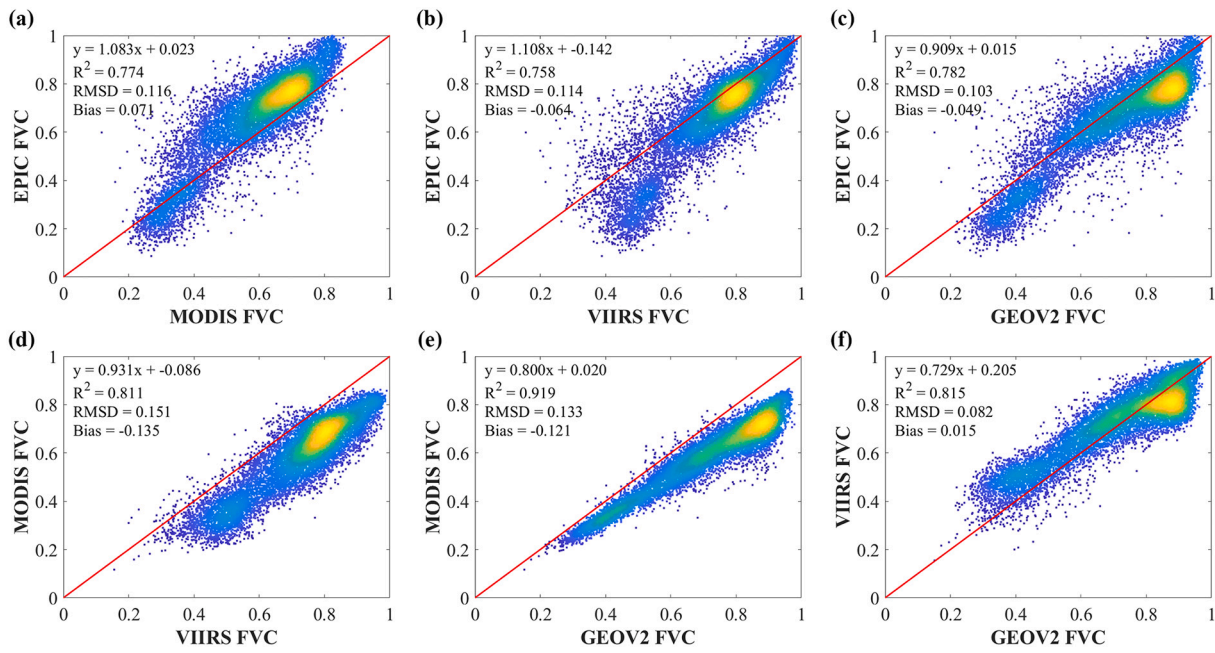
Fig. 9. Per-pixel comparison for FVC from EPIC, MODIS, VIIRS, and GEOV2 at 10 km resolution over the Mississippi region on or containing 10 June 2016. Red lines on each plot represent the 1:1 line and the colors of the data cloud represent the density of data ranging from yellow (highest) to blue (lowest). (For interpretation of the references to colour in this figure legend, the reader is referred to the web version of this article.)
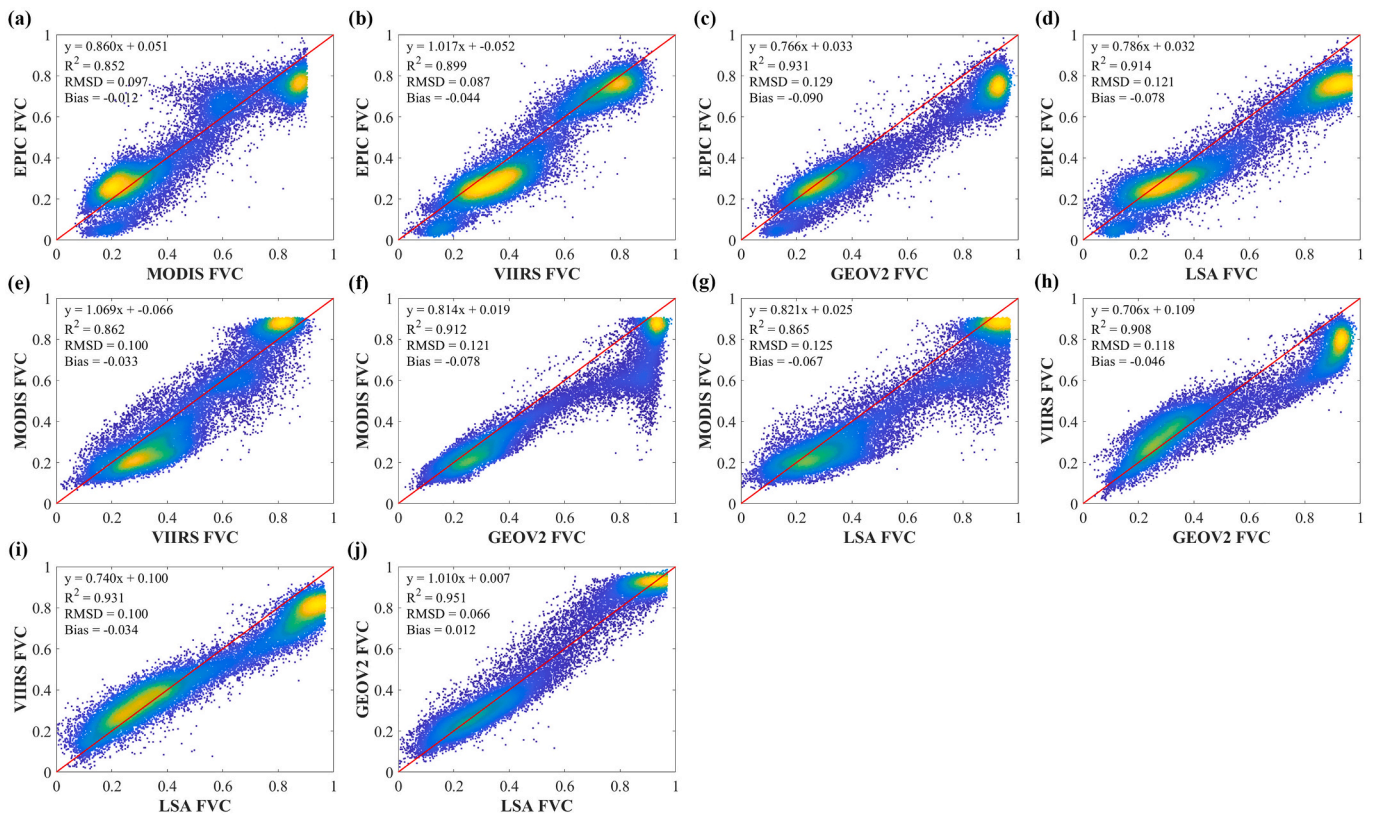

Fig. 10. Per-pixel comparison for FVC from EPIC, MODIS, VIIRS, GEOV2, and LSA at 10 km resolution over the two Africa regions on or containing 30 April 2016. Red lines on each plot represent the 1:1 line and the colors of the data cloud represent the density of data ranging from yellow (highest) to blue (lowest). (For interpretation of the references to colour in this figure legend, the reader is referred to the web version of this article.)

4.3.3. Comparison of time series

Comparison of FVC time-series from EPIC, MODIS, VIIRS, GEOV2, and LSA over the Mississippi (Fig. 13(a)) and southern Africa (Fig. 13

(b)) regions were conducted over 2016. The five products show similar FVC temporal dynamics. The seasonality differences of the north and south hemispheres are obvious in Fig. 13, as are the much higher peak
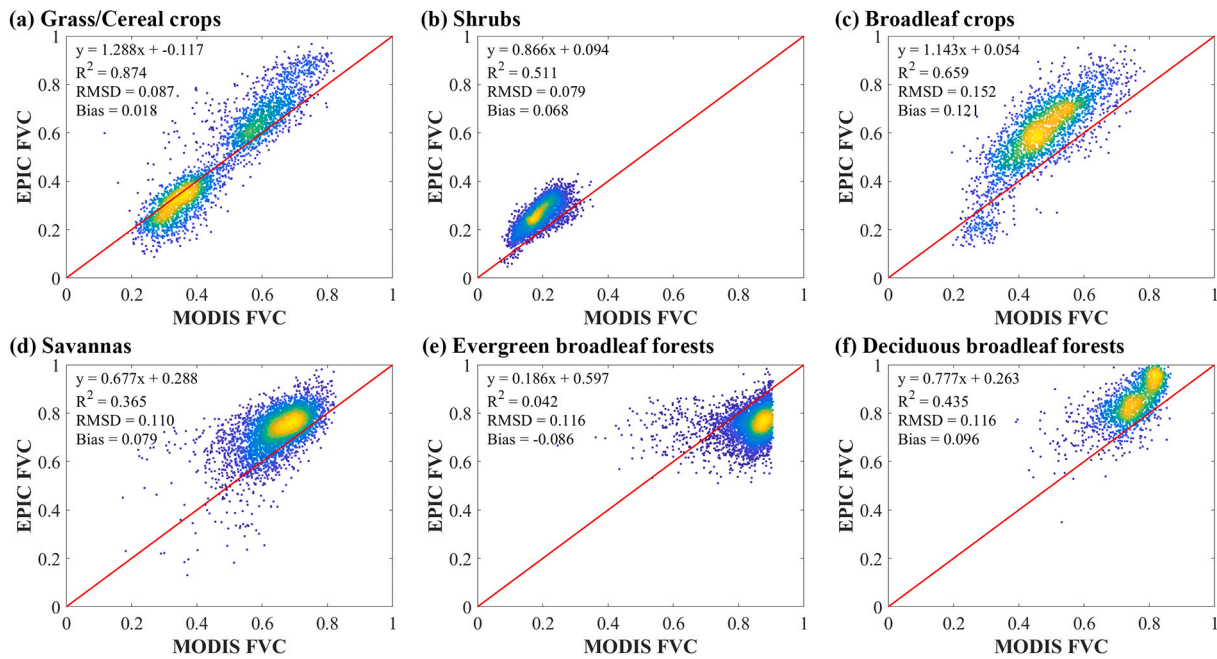
Fig. 11. Per-pixel comparison between EPIC FVC and MODIS FVC retrievals of six major land cover types in the Mississippi region and the two Africa regions. Data in (a), (c), (d), and (f) are from the Mississippi region. Data in (b) and (e) are from the southern and central Africa regions, respectively. The red line on each plot is the 1:1 line. (For interpretation of the references to colour in this figure legend, the reader is referred to the web version of this article.)
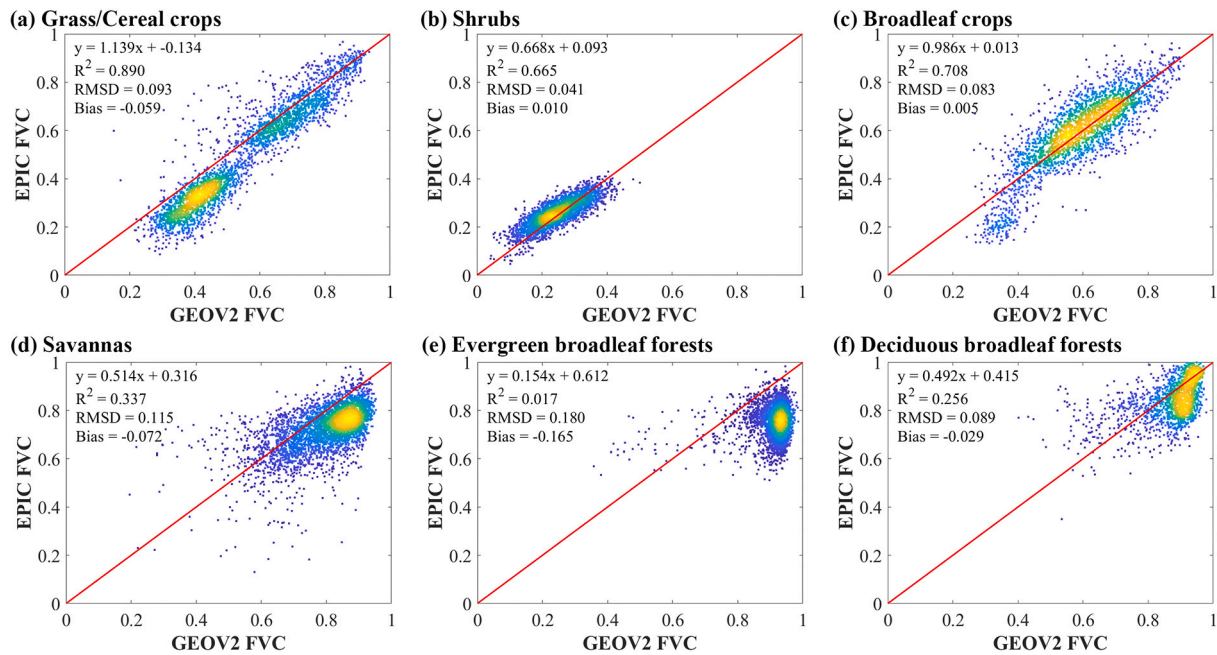

Fig. 12. Per-pixel comparison between EPIC FVC and GEOV2 FVC. The same as Fig. 11 except that EPIC retrievals are compared with GEOV2 retrievals.

FVC values experienced across the Mississippi region when compared to the southern Africa region.

EPIC FVC has more fluctuations than others due to the missing data caused by the cloud. The FVC estimates from VIIRS, GEOV2, and LSA are smoother than those based on MODIS and EPIC. This is because VIIRS, GEOV2, and LSA have been smoothed to remove atmospheric contamination observations and to fill gaps (Tables 1 and 2). Herein, no smoothing filter or composite window was applied to EPIC FVC. In Fig. 13(a), FVC has a substantial decrease around DOY 225, which is captured by both quasi-daily EPIC and 8-day composite MODIS FVC estimates. This rapid FVC decrease is observed using VIIRS with an

approximate 10-day delay mainly due to the daily rolling and 15-week smoothing schemes (Table 1). GEOV2 doesn't capture this signature.

In Fig. 13(b), EPIC FVC is lower than VIIRS FVC when FVC is low. Research has revealed that both VIIRS FVC (Ding and Zhu, 2018 their Fig. 17) and GEOV2 FVC (Pérez et al., 2019 their Fig. 46 and Annex III) overestimate FVC when it is low (i.e., FVC < 0.3) when compared with field-based results. In Fig. 13(a), EPIC FVC is substantially lower than VIIRS and GEOV2 before DOY 100 when vegetation coverage is sparse. In Fig. 13(b), EPIC FVC is lower than VIIRS FVC and GEOV2 FVC after DOY 200. This means that EPIC FVC reduced the severity of the overestimation problem compared to VIIRS and GEOV2 FVC when FVC is
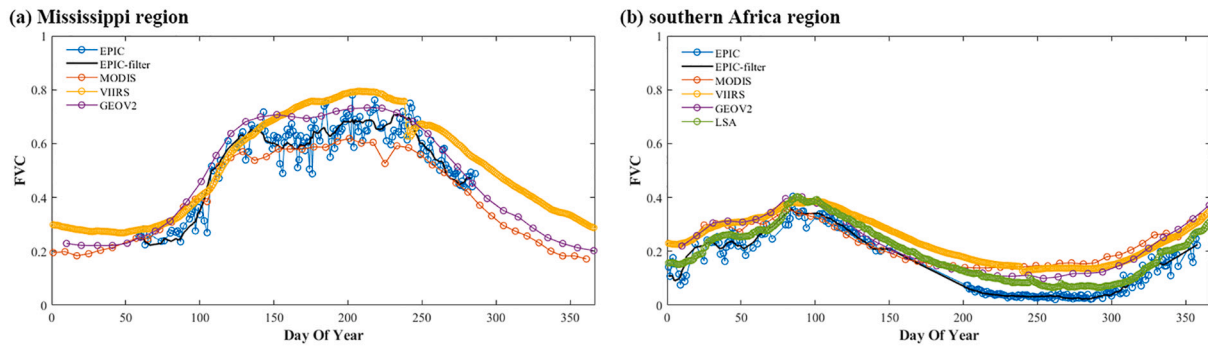
Fig. 13. The time series of daily (366 products/per year) EPIC, VIIRS, and LSA FVC and low-frequency MODIS (8-day; 45 products/per year) and GEOV2 (10-day; 36 products/per year) FVC in 2016. After being smoothed using a 30-day Savitzky-Golay filter, the quasi-daily EPIC FVC is shown as the black curve denoted as "EPIC-filter" in the legend. (a) and (b) are the Mississippi region and southern Africa region, respectively.
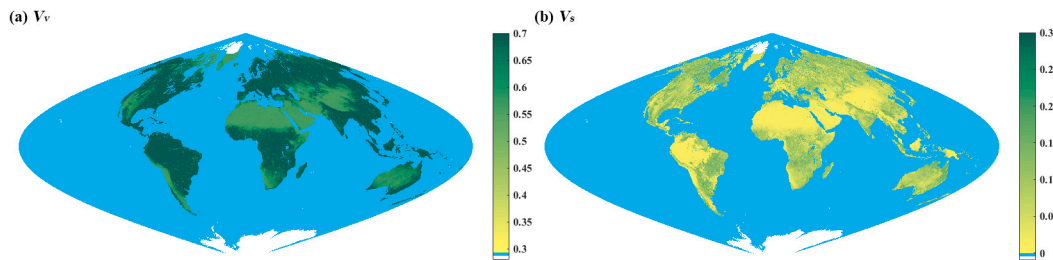

Fig. 14. Global distribution of (a) V_v and (b) V_s in 2016. The blue colour in these images represents the ocean and white is for filled value. The data are shown in the same sinusoidal projection as the EPIC data are provided. Note while (a) and (b) use the same colour range they are scaled differently. (For interpretation of the references to colour in this figure legend, the reader is referred to the web version of this article.)

low. In the southern Africa region (Fig. 13(b)) which is mainly covered by grass/cereal crops and shrubs (Fig. 5(b)), EPIC has the most consistency in terms of FVC magnitude with LSA.

4.4. Global pattern of EPIC FVC

Global V_v and V_s images were produced in this study (Fig. 14). A simple linear spatial interpolation method was used to fill in the gaps due to data quality. Table 4 presents the global average and standard deviation of V_v and V_s for each land cover type. Broadleaf crops, savannas, and forests (i.e., EBF, DBF, evergreen needleleaf forests (ENF), and deciduous needleleaf forests (DNF)) have higher V_v than grass/cereal crops and shrubs with relatively less standard deviation. The V_v differences among different land cover types are mainly due to the differences in vegetation optical properties and structures. Considering that both broadleaf crops and forests usually have very dense vegetation coverage conditions and global averaged LAIs are all greater than 2.0 (Yan et al., 2016b their Table 3), this explains the similarity of V_v for broadleaf crops and forests. Although savannas exhibit a smaller global

Table 4
Land cover-based information of global V_v and V_s estimation. The mean values and standard deviations (Std) are listed. The numbers in parentheses are the number of 10 km pixels in each land cover type.

Land Cover Type	V_v		V_s	
	Mean	Std	Mean	Std
Grass/Cereal crops (321,605)	0.661	0.044	0.071	0.038
Shrubs (217,080)	0.636	0.048	0.083	0.037
Broadleaf crops (33,220)	0.692	0.019	0.087	0.038
Savannas (245,681)	0.689	0.018	0.095	0.038
Evergreen broadleaf forests (EBF; 146,756)	0.696	0.011	0.043	0.037
Deciduous broadleaf forests (DBF; 52,974)	0.697	0.010	0.077	0.040
Evergreen needleleaf forests (ENF; 64,393)	0.693	0.013	0.090	0.039
Deciduous needleleaf forests (DNF; 18,390)	0.695	0.007	0.086	0.028

averaged LAI (1.46) than broadleaf crops and forests, it is still greater than grass/cereal crops (1.32) and shrubs (0.21; Yan et al., 2016b their Table 3), which results in that the global averaged V_v for savannas being greater than V_v for grass/cereal crops and shrubs, and less than the V_v for broadleaf crops and forests. The standard deviations of V_s are higher than the corresponding standard deviations of V_v for all land cover types (Table 4) as the soil type varies spatially and soil moisture varies spatial-temporally within each vegetation type affecting the background reflectivity (Idso et al., 1975).

Every 3 months global maximum FVC from EPIC is presented in Fig. 15. The Amazon Forest, Congo Forest, and forest in Southeast Asia are all located in the equatorial area and are mainly covered by EBF with high FVC values in the whole year. The maximum FVC value is over 0.9 in the 3rd season (July ~ September; Fig. 15(c)). While the east of China, east of North America, and Europe are located in the subtropical and temperate zone in the northern hemisphere, where most vegetation is grass/cereal crops, broadleaf crops, savannas, or DBF. FVC values for these areas in the 2nd (April ~ June; Fig. 15(b)) and 3rd (July ~ September; Fig. 15(c)) seasons are substantially higher than others (Fig. 15(a) and (d)). The maximum appears in the 3rd season in the boreal summer.

5. Discussion

5.1. The angle issues in MultiHSVI

The key parameters for the two-endmember model, V_v and V_s, are both assumed to have a weak dependence on VZA herein. V_v is defined as the vegetation index for a homogenous, fully-covered vegetated pixel. Due to the saturation problem of BRF in NIR bands, the variation range of EVI2 decreased with increasing LAI. Studies have shown that the yearly averaged EVI, which is highly consistent with EVI2 (Jiang et al., 2008), over the nearly homogenous and fully-covered Amazon Forest is about 0.55 and the seasonal variation is about 0.06 (de Moura et al.,
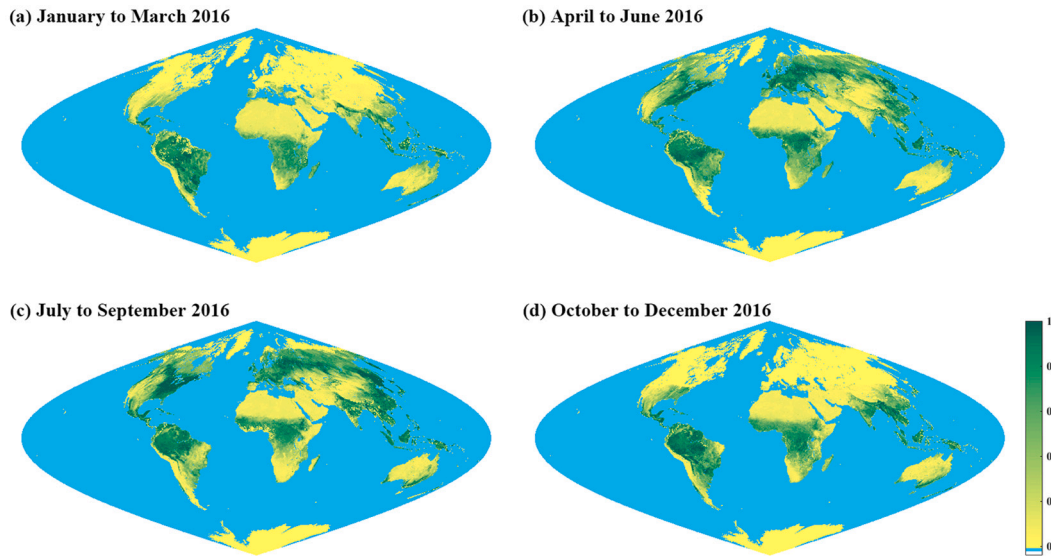
Fig. 15. Global FVC distributions in 2016. The seasonal maximum FVC is presented. (a) ~ (d) show the 4 seasons, respectively. The blue colour in these images represents the ocean and white is for filled value. The data are shown in the same sinusoidal projection as the EPIC data are provided. (For interpretation of the references to colour in this figure legend, the reader is referred to the web version of this article.)

2017 their Fig. 14; Hilker et al., 2017 their Fig. 12). This amount of variation in V_v (i.e., assuming that the EVI2 of Amazon Forest represents V_v) can lead to an absolute error of 0.08 in the estimation of Amazon Forest FVC via the EVI2-based two-endmember mixture model (i.e., EVI2 = 0.55; V_v = 0.696, V_s = 0.034 according to Table 4). Therefore, the FVC estimation error caused by the variation of V_v with VZA is less than 0.08 (in FVC units) over Amazon Forest, and should be even less over other vegetated areas. This is because that the variation of V_v has more impact over dense vegetation based on model simulation (i.e., typically FVC > 0.6; Mu et al., 2021 their Fig. 12; Yan et al., 2021 their Fig. 12), with the Amazon Forest being an example of extremely dense

vegetation. As for V_s, by assuming the soil background as Lambertian herein (Widlowski et al., 2015; Widlowski et al., 2013), it is independent of VZA.

When estimating V_v and V_s, MultiHSVI assumes that there is no angle dependence for the G function and Ω. According to model simulation, G decreases with increasing VZA for most LADs except for the spherical and erectophile distributions and is constant for spherical LAD for a variety of vegetation including soybean, wheat, sorghum, oaks, and grass (Goel and Strebel, 1984; Mu et al., 2018 their Fig. 9). However, Ω increases with increasing VZA for most vegetation types in theory as has been shown for data collected and model validated over crops (i.e.,
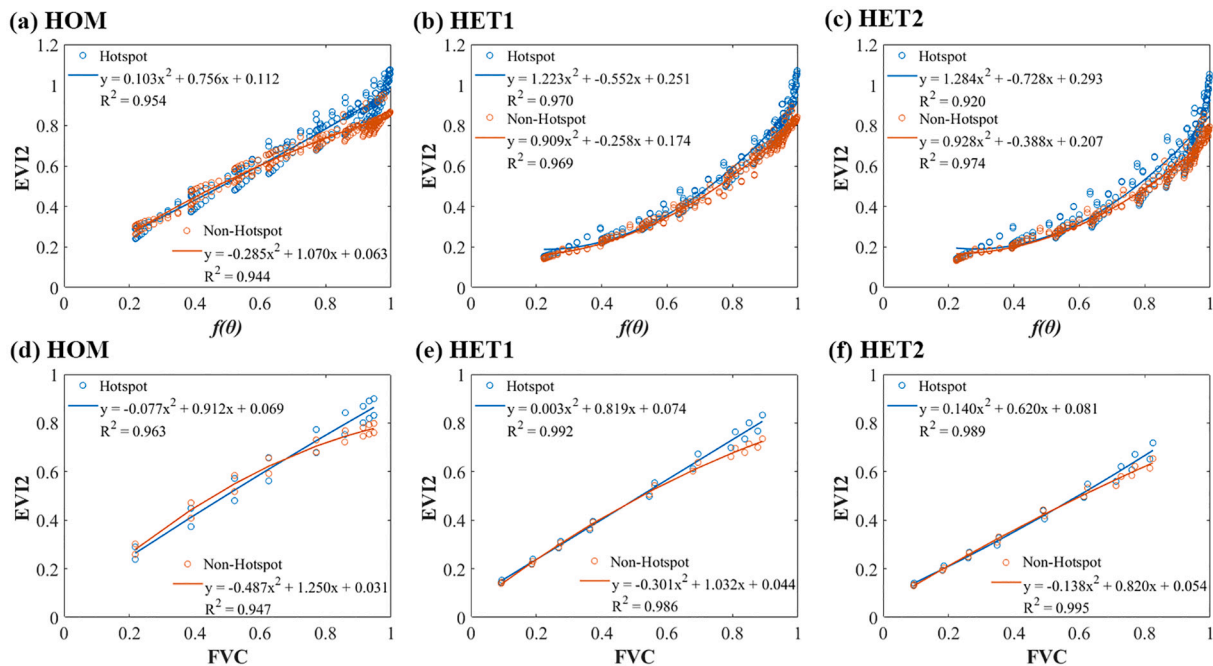

Fig. 16. Analysis of EVI2 versus vegetation cover using the simulated EPIC dataset based on the LESS model (described in Section 2.2). (a) ~ (c) are EVI2 versus directional vegetation cover $f(\theta)$ for the homogeneous scene (HOM), the heterogeneous scene with spherical crowns (HET1), and the heterogeneous scene with spherical and cylinder-shaped crowns (HET2), respectively. (d) ~ (f) are EVI2 versus FVC in HOM, HET1, and HET2, respectively. SZA is 40° for EVI2 in non-Hotspot direction.

tested on maize, soybean, sorghum), and forests (i.e., aspen, Jack pine, black spruce), and grasslands (Peng et al., 2018 their Fig. 2; Fang et al., 2018 their Fig. 7; Braghiere et al., 2020; Kucharik et al., 1999 their Fig. 5; Nouvellon et al., 2000). Thus, the variations of G and Ω cancel each other out to a certain extent when multiplied together and their overall influences are reduced (Sec. S3). The variation of $G \bullet \Omega$ is small and negligible ($\approx 6\%$; Table S5) when compared to the corresponding variation of $1/\cos\theta$ (19%) for large VZA ($45° \leq VZA \leq 55°$). The error caused by 5% variation of $G \bullet \Omega$ is less than 2% in FVC units (Mu et al., 2018 their Fig. 11) across a wide range of vegetation cover.

5.2. The analysis of MultiHSVI FVC estimation methods based on model simulation

5.2.1. The advantage of hotspot observations

Herein, we improved the MultiVI method (Mu et al., 2018) by introducing the Hotspot EVI2 data into V_v and V_s estimation and the FVC retrieval. Section 3.1 explains the theoretical advantage of using Hotspot observations and here we augment this theory by analysis of the simulated dataset described in Section 2.2. Fig. 16 shows the $V(\theta)$ in the Hotspot directions and non-Hotspot directions (SZA = 40°) versus $f(\theta)$ when VZA varies from 0° to 60°. Based on the simulated dataset, the relationship between $V(\theta)$ and $f(\theta)$ are non-linear especially for densely vegetated and highly heterogeneous vegetation conditions (Fig. 16(b) and (c)) at both the Hotspot and non-Hotspot directions. This illustrates the feasibility of using the non-linear mixture model (Eq. (5)) to estimate V_v and V_s.

However, the relationship between nadir Hotspot EVI2 and FVC is generally linear whereas non-Hotspot EVI2 and FVC is still nonlinear at nadir (Fig. 16(d) ~ (f)). The absolute value of the first term of the quadratic coefficients of nadir Hotspot EVI2 versus FVC (0.077– 0.140) are smaller than non-Hotspot EVI2's (0.138– 0.487) and the R^2 is also larger for the Hotspot cases when compared to the non-Hotspot cases (Fig. 16(d) ~ (f)). The variation of nadir non-Hotspot EVI2 is due to both vegetation structure and the spectral difference between sunlit and shaded components. However, for nadir Hotspot EVI2 there is no shaded vegetation nor shaded background components, so vegetation structure is the major impact factor. This illustrates the feasibility of using the two-endmember linear mixture model (Eq. (1)) when estimating FVC based on the EPIC Hotspot dataset.

5.2.2. The feasibility of angle selection in V_v and V_s estimation

Observations with large VZAs ($45° \leq SZA \leq 55°$) were used in MultiHSVI for V_v and V_s estimation. Fig. 17 analyzes the relative difference of EVI2 with large VZAs according to LAI and how it impacts the estimation of V_v and V_s. Fig. 17(a) presents the relative difference between $V(45°)$ and $V(55°)$. A larger relative difference between $V(45°)$ and $V(55°)$ increase the stability of Eq. (9), which can help the estimation of V_v and V_s. Hotspot EVI2 has over 0.090 (± 0.027) relative differences for the range of LAI (i.e., 0.5 to 6.0; Fig. 17(a) blue line). As we can see, EVI2 in non-Hotspot directions only has relative differences below 0.100 (± 0.040; Fig. 17(a) orange line). Therefore, Hotspot EVI2 is more sensitive to the VZA than non-Hotspot ones at large VZAs, and is superior in solving Eq. (9) for V_v and V_s estimation. A larger relative differences appear in low and middle LAI ranges (representing sparse and medium vegetation conditions herein, i.e., LAI from 0.5 to 4.0; Fig. 17(a)).

To show how these relative differences affects the V_v and V_s estimation, Fig. 17(b) presents the MultiHSVI estimated V_v and V_s based on the EVI2 simulated using each previously described LAI increment from 0.5 to 6.0. The V_v and V_s estimated from EVI2 based on LAI from 0.5 to 6.0 is taken as the references (dashed horizontal lines in Fig. 17(b)). We can see that when LAI is relatively low (LAI ≤ 2.0; representing sparse vegetation conditions herein), V_v is usually underestimated and has a relatively large variation (blue error bar in Fig. 17(b)) due to different vegetation distributions. When LAI is relatively large (LAI ≥ 4.0; representing dense vegetation conditions herein), since the EVI2 relative differences are small and EVI2 almost saturates, the V_v estimations horizontally asymptote. On average, V_v estimated from the LAI simulations conducted herein will cause a relative error of 11.5%. Meanwhile, the estimations for V_s have large uncertainty. The difference between V_s and the reference is 0.054, which means the relative error can reach 114.6%. These show that the V_v and V_s estimations have relatively large uncertainty in sparse and dense vegetation areas, respectively (Fig. 17 (b)). We can conclude that V_v and V_s estimation using observations at a single LAI level introduces unacceptable uncertainty. Therefore, when implementing MultiHSVI using EPIC data, we used the Hotspot EVI2 over the entire 2016 to guarantee a sufficiently large range of vegetation coverage (and LAI) conditions for V_v and V_s estimation.

5.2.3. The uncertainty of SZA variation in FVC estimation

Since EPIC cannot provide nadir Hotspot observations for all pixels, Fig. 18 presents the uncertainty (RMSD) of FVC retrieval due to SZA
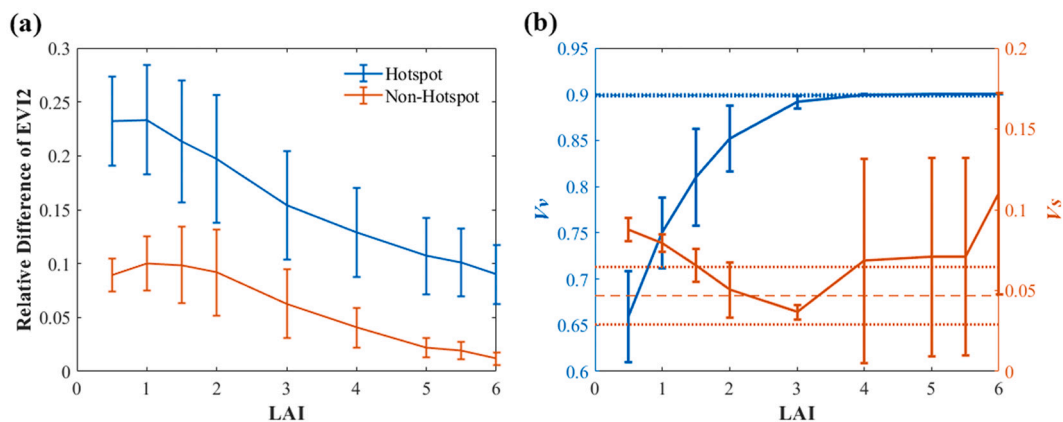

Fig. 17. Analysis of EVI2 relative differences with large VZA (45° and 55°) and its impact using the simulated EPIC dataset based on the LESS model (described in Section 2.2). (a) shows the relative differences between $V(45°)$ and $V(55°)$ and (b) shows the V_v and V_s estimation according to each LAI level. Error bars in both (a) and (b) represent the positive and negative standard deviation around the mean. The blue curve in (b) represents V_v (refer to the left Y-axis) while the orange curve is for V_s (right Y-axis). Dashed horizontal lines are V_v and V_s results estimated using the MultiHSVI method and VIs based on LAI from 0.5 to 6.0. The horizontal dotted lines show the mean $\pm$ standard deviation for V_v and V_s estimates. Note that the mean of V_v estimates (blue dashed line) is 0.899 and the standard deviation of this V_v is 0.001. SZA = 40° for EVI2 in non-Hotspot direction. (For interpretation of the references to colour in this figure legend, the reader is referred to the web version of this article.)
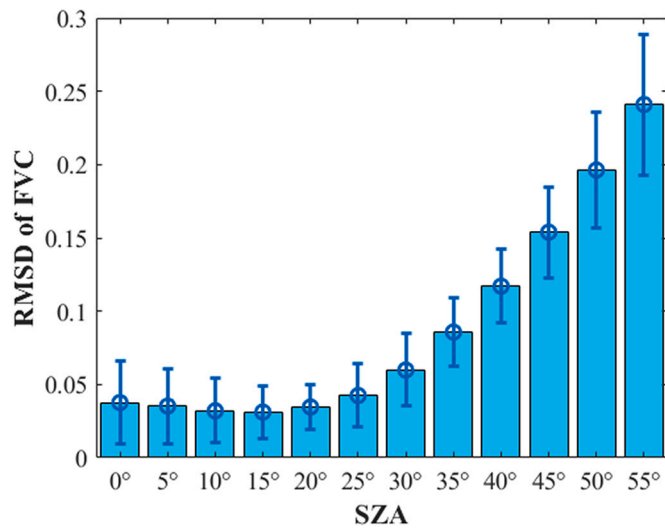
Fig. 18. Uncertainty of FVC estimation using the MultiHSVI method due to SZA variation. FVC was estimated with Hotspot EVI2 at different SZAs over a wide range of vegetation conditions (i.e., LAI from 0.5 to 6). Each light blue bar indicates the mean RMSD value for each SZA; each dark blue error bar represents the positive/negative one standard deviation. (For interpretation of the references to colour in this figure legend, the reader is referred to the web version of this article.)

variation. In the modeling to generate Fig. 18, V_v and V_s are the same as Fig. 7(a), only SZA varies when estimating FVC (Eq. (10)). Generally, uncertainty is essentially constant for SZA ranging from 0° to 20°, and beyond that uncertainty increased markedly as SZA increases (Fig. 18). The FVC estimated with EVI2 at SZA greater than 45° is specially marked in the quality file, considering that the current FVC products' uncertainties are all less than 0.20 (Table 1).

5.2.4. The influence of different VI on MultiHSVI

Theoretically, MultiHSVI is suitable to all VIs that can distinguish vegetation and background. Herein, we take EVI2 as an example to analyze its advantage, feasibility, and uncertainty and to produce EPIC FVC based on the simulated EPIC dataset in Section 2.2. Fig. 19 presents the retrieved FVC results when EVI2, NDVI, and DVI are applied to MultiHSVI. As shown in Fig. 19(a), both EVI2 and NDVI have good accuracy with RMSD of 0.037 and 0.030, respectively. However, NDVI is very sensitive to soil background (Huete, 1988; Rocha and Shaver, 2009), when soil reflectance changed, the RMSD for NDVI case increases to 0.124 while EVI2 still has an RMSD of 0.034 (Fig. 19(b)). DVI results

in less accuracy than EVI2 and NDVI, with RMSD of 0.074 and 0.114 for the two different soil backgrounds. The R^2 for all three VIs over the two soil backgrounds is greater than 0.95 (Fig. 19). The p-value in the significance t-test with a confidence level equal to 90% is less than 0.001.

5.3. The feasibility of global quasi-daily FVC Production from EPIC data

According to Sections 3.2 and 3.3, the number of selected observations ($45° \leq SZA \leq 55°$; dark blue in Fig. 1(a)) for V_v and V_s retrieval is less than 2/day on average from September to April and around 2/day from May to August. To maintain enough observations for solving Eq. (9) and to obtain a stable and efficient solution, observations in a time series (e.g., all 2016) are necessary to retrieve V_v and V_s globally. In theory, at least one observation per day is required for daily FVC calculation based on Eq. (10). Areas between 78°N and 76°S, have sufficient observations for FVC retrieval based on EPIC data in 2016 (Fig. 1 (b)).

When considering cloud (Delgado-Bonal et al., 2020; Wilson and Jetz, 2016), smoke, and other atmospheric conditions, there are pixels without daily EPIC observations. Thus we obtained quasi-daily FVC product through MultiHSVI based on EPIC data (i.e., for a single pixel, it might not has FVC result every day). Since EPIC observes the entire sunlit Earth's surface up to 13 to 23 times every day (Marshak et al., 2018), it will increase the temporal frequency of the global FVC products when compared to LEO-based FVC products (generally 8-days and longer). Additionally, EPIC has the advantage of global coverage when compared to GEO satellites (Song et al., 2018).

5.4. The Prospect of EPIC FVC

MultiHSVI is used to produce global 10 km quasi-daily FVC products with the EPIC dataset, which is helpful to climate change, vegetation phenology, bushfire monitoring, and other researches that consider vegetation dynamics. This coarse spatial resolution FVC products can be used in terrestrial climate and vegetation models such as the regional climate model (RegCM3; Pal et al., 2007), the Weather Research and Forecasting (WRF; Skamarock et al., 2008), the Lund-Potsdam-Jena Dynamic Global Vegetation Model (LPJ-DGVM; Sitch et al., 2003). It is also able to work with satellite-based atmospheric carbon dioxide products (Pan et al., 2021 their Table 1). This implicates that the high-frequency vegetation product from EPIC can be used to analyze the carbon cycle between the atmosphere and biosphere. According to Fig. 13, EPIC FVC can capture quasi-daily vegetation dynamics over the global land surface, which is conductive to the terrestrial vegetation phenology analysis (Ahl et al., 2006; Sobrino et al., 2013; Yan et al., 2016a).
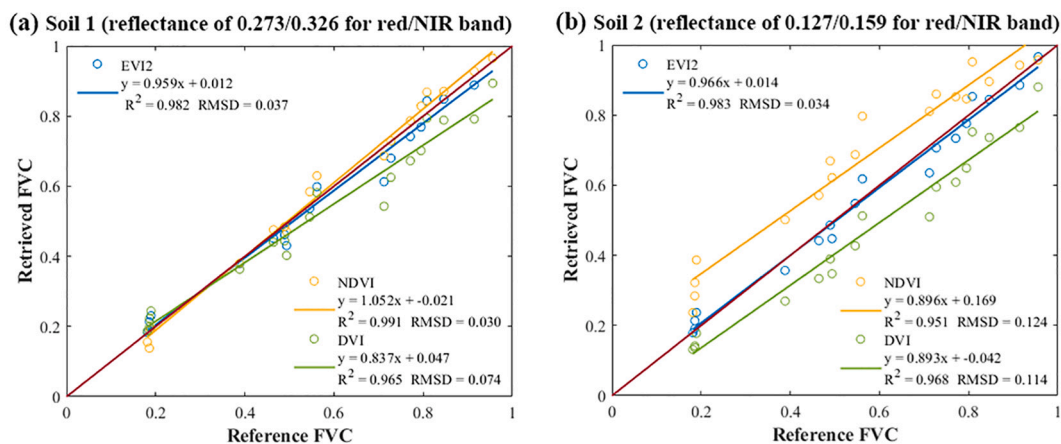

Fig. 19. Analysis of FVC estimation using the MultiHSVI method with EVI2, NDVI, and DVI. Comparison of retrieved FVC versus the reference for a range of vegetation conditions (i.e., LAI = 1.0, 3.0, 5.0). The experiment compares the FVC retrieved under two different soil backgrounds.

6. Conclusion

Fractional Vegetation Cover (FVC) is a basic biophysical structural parameter and is widely used in climate and land-surface research. However, the compromise among temporal frequency, spatial resolution, and spatial coverage of current FVC products (i.e., MODIS, VIIRS, GEOV2, and LSA) limit their utility in some circumstances.

In this study, an improved FVC estimation method based on Multi-SZA HotSpot VI (MultiHSVI) was developed, which enabled production of a global quasi-daily FVC estimates using the recently published EPIC near Hotspot dataset. MultiHSVI uses the multi-SZA Hotspot EVI2 from EPIC and the combination of EVI2-based two-endmember mixture model and gap fraction model to estimate FVC and the two key parameters (V_v and V_s) without depending on any prior knowledge. The uncertainty (RMSD) of MultiHSVI FVC was around 0.050 according to the analyses using the simulated dataset for three typical scenes (i.e., a homogeneous scene, a heterogeneous scene with spherical crowns, and a heterogeneous scene with spherical and cylinder-shaped crowns). By taking the field-based Landsat FVC as the reference, EPIC FVC has an RMSD of 0.043 with a bias of 0.012 in the Saihanba area in northern China. The R^2 between EPIC MultiHSVI FVC and FVC from MODIS, VIIRS, GEOV2, or LSA, is larger than 0.758, and the difference (RMSD) is less than 0.129 in FVC units. The comparisons were conducted at the Mississippi region in the northern hemisphere, the southern Africa region in the southern hemisphere, and the central Africa region near the equator.

Our results demonstrate that EPIC FVC can be accurately generated, and it increases the temporal frequency of large-scale satellite-based FVC products. The global quasi-daily EPIC FVC is expected to improve climate change, vegetation phenology, and other related terrestrial research.

Declaration of Competing Interest

The authors declare that they have no known competing financial interests or personal relationships that could have appeared to influence the work reported in this paper.

Acknowledgments

Appendix A. Supplementary data

Supplementary data to this article can be found online at https://doi.org/10.1016/j.rse.2021.112835.

References

Ahl, D.E., Gower, S.T., Burrows, S.N., Shabanov, N.V., Myneni, R.B., Knyazikhin, Y., 2006. Monitoring spring canopy phenology of a deciduous broadleaf Forest using MODIS. Remote Sens. Environ. 104, 88–95.

Baret, F., Weiss, M., 2019. Algorithm Theoretical Basis Document, Leaf Area Index (LAI), Fraction of Absorbed Photosynthetically Active Radiation (FAPAR), Fraction of Green Vegetation Cover (FCOVER), Collection 1km, Version 2. In. A. Verger (Ed.), Copernicus Global Land Operations "Vegetation and Energy" " Cglops-1": Copernicus. https://land.copernicus.eu/global/sites/cgls.vito.be/files/products/CGLOPS1_ATBD_FCOVER1km-V2_I1.41.pdf (last accessed on 12/November/2021).

Baret, F., Weiss, M., Lacaze, R., Camacho, F., Makhmara, H., Pacholcyzk, P., Smets, B., 2013. GEOV1: LAI and FAPAR essential climate variables and FCOVER global time series capitalizing over existing products. Part1: principles of development and production. Remote Sens. Environ. 137, 299–309.

Barnes, P., Wilson, B.R., Reid, N., Bayerlein, L., Koen, T.B., Olupot, G., 2015. Examining the impact of shade on above-ground biomass and normalized difference vegetation index of C3 and C4 grass species in North-Western NSW, Australia. Grass Forage Sci. 70, 324–334.

Braghiere, R.K., Quaife, T., Black, E., Ryu, Y., Chen, Q., De Kauwe, M.G., Baldocchi, D., 2020. Influence of sun zenith angle on canopy clumping and the resulting impacts on photosynthesis. Agricult. For. Meteorol. 291, 108065.

Camacho, F., Cernicharo, J., Lacaze, R., Baret, F., Weiss, M., 2013. GEOV1: LAI, FAPAR essential climate variables and FCOVER global time series capitalizing over existing products. Part 2: validation and Intercomparison with reference products. Remote Sens. Environ. 137, 310–329.

Camacho, F., García-Haro, F.J., Sánchez-Zapero, J., Fuster, B., 2018. The Eumetsat Satellite Application Facility on Land Surface Analysis, Validation Report, MSG/SEVIRI, Vegetation Parameters (VEGA), Version 3.1. https://nextcloud.lsasvcs.ipma.pt/s/eLqXeyDd3NbQNej?dir=undefined&openfile=105701 (last accessed on 24/June/2021).

Carlson, T.N., Sanchez-Azofeifa, G.A., 1999. Satellite remote sensing of land use changes in and around San José, Costa Rica. Remote Sens. Environ. 70, 247–256.

Cerstl, S., Simmer, C., 1986. Radiation physics and modelling for off-nadir satellite-sensing of non-lambertian surfaces. Remote Sens. Environ. 20, 1–29.

Chen, J.M., Leblanc, S.G., Miller, J.R., Freemantle, J., Loechel, S.E., Walthall, C.L., Innanen, K.A., White, H.P., 1999. Compact airborne spectrographic imager (CASI) used for mapping biophysical parameters of boreal forests. J. Geophys. Res.-Atmos. 104, 27945–27958.

Chen, J.M., Menges, C.H., Leblanc, S.G., 2005. Global mapping of foliage clumping index using multi-angular satellite data. Remote Sens. Environ. 97, 447–457.

Choudhury, B.J., Ahmed, N.U., Idso, S.B., Reginato, R.J., Daughtry, C.S.T., 1994. Relations between evaporation coefficients and vegetation indices studied by model simulations. Remote Sens. Environ. 50, 1–17.

Clark, B.E., Fanale, F.P., Salisbury, J.W., 1992. Meteorite-asteroid spectral comparison: the effects of comminution, melting, and recrystallization. Icarus 97, 288–297.

Crowther, T.W., Glick, H.B., Covey, K.R., Bettigole, C., Maynard, D.S., Thomas, S.M., Smith, J.R., Hintler, G., Duguid, M.C., Amatulli, G., Tuanmu, M.N., Jetz, W., Salas, C., Stam, C., Piotto, D., Tavani, R., Green, S., Bruce, G., Williams, S.J., Wiser, S.K., Huber, M.O., Hengeveld, G.M., Nabuurs, G.J., Tikhonova, E., Borchardt, P., Li, C.F., Powrie, L.W., Fischer, M., Hemp, A., Homeier, J., Cho, P., Vibrans, A.C., Umunay, P.M., Piao, S.L., Rowe, C.W., Ashton, M.S., Crane, P.R., Bradford, M.A., 2015. Mapping tree density at a global scale. Nature 525, 201–205.

CTOS, 2010. Implementation Plan for the Global Observing System for Climate in Support of the UNFCCC; GCOS Rep. 138; CTOS: Geneva, Switzerland. https://library.wmo.int/doc_num.php?explnum_id=3851 (last accessed on 12/November/2021).

de Moura, Y.M., Galvão, L.S., Hilker, T., Wu, J., Saleska, S., do Amaral, C.H., Nelson, B. W., Lopes, A.P., Wiedeman, K.K., Prohaska, N., de Oliveira, R.C., Machado, C.B., Aragão, L.E.O.C., 2017. Spectral analysis of Amazon canopy phenology during the dry season using a tower hyperspectral camera and MODIS observations. ISPRS J. Photogramm. Remote Sens. 131, 52–64.

Deardorff, J., 1978. Efficient prediction of ground surface temperature and moisture, with inclusion of a layer of vegetation. J. Geophys. Res. Oceans 83, 1889–1903.

DeFries, R.S., Townshend, J.R.G., Hansen, M.C., 1999. Continuous fields of vegetation characteristics at the global scale at 1-km resolution. J. Geophys. Res.-Atmos. 104, 16911–16923.

Delgado-Bonal, A., Marshak, A., Yang, Y., Oreopoulos, L., 2020. Daytime variability of cloud fraction from DSCOVR/EPIC observations. J. Geophys. Res.-Atmos. 125 e2019JD031488.

Ding, H., Zhu, Y., 2018. NDE Vegetation Products System (NVPS) Green Vegetation Fraction (GVF) NOAA-Unique Product, Algorithm Theoretical Basis Document Version 4.0. NOAA/NESDIS/OSPO. https://viirsland.gsfc.nasa.gov/Products/NOAA/GVF.html (last accessed on 12/November/2021).

Ding, Y., Zheng, X., Zhao, K., Xin, X., Liu, H., 2016. Quantifying the impact of Ndvisoil determination methods and Ndvisoil variability on the estimation of fractional vegetation cover in Northeast China. Remote Sens. 8, 29.

Donohue, R.J., Hume, I.H., Roderick, M.L., McVicar, T.R., Beringer, J., Hutley, L., Gallant, J.C., Austin, J., van Gorsel, E., Cleverly, J., Meyer, W.S., Arndt, S.K., 2014. Evaluation of the remote-sensing-based diffuse model for estimating photosynthesis of vegetation. Remote Sens. Environ. 155, 349–365.

Fang, H., Ye, Y., Liu, W., Wei, S., Ma, L., 2018. Continuous estimation of canopy leaf area index (LAI) and clumping index over broadleaf crop fields: an investigation of the PASTIS-57 instrument and smartphone applications. Agricult. For. Meteorol. 253, 48–61.

Fang, H., Baret, F., Plummer, S., Schaepman-Strub, G., 2019. An overview of global leaf area index (LAI): methods, products, validation, and applications. Rev. Geophys. 57, 739–799.

Foley, J.A., Prentice, I.C., Ramankutty, N., Levis, S., Pollard, D., Sitch, S., Haxeltine, A., 1996. An integrated biosphere model of land surface processes, terrestrial carbon balance, and vegetation dynamics. Glob. Biogeochem. Cycles 10, 603–628.

Friedl, M.A., Sulla-Menashe, D., Tan, B., Schneider, A., Ramankutty, N., Sibley, A., Huang, X., 2010. MODIS collection 5 global land cover: algorithm refinements and characterization of new datasets. Remote Sens. Environ. 114, 168–182.

Gao, L., Wang, X., Johnson, B.A., Tian, Q., Wang, Y., Verrelst, J., Mu, X., Gu, X., 2020. Remote sensing algorithms for estimation of fractional vegetation cover using pure vegetation index values: A review. ISPRS J. Photogramm. Remote Sens. 159, 364–377.

García-Haro, F.J., Camacho, F., Martínez, B., Campos-Taberner, M., Fuster, B., Sánchez-Zapero, J., Gilabert, M.A., 2019. Climate data records of vegetation variables from

geostationary SEVIRI/MSG data: products, algorithms and applications. Remote Sens. 11, 2103.

Garrity, D., Bindraban, P., 2004. A Globally Distributed Soil Spectral Library Visible near Infrared Diffuse Reflectance Spectra. In World Agroforestry Centre (ICRAF) & ISRIC - World Soil Information. Nairobi, Kenya. https://worldagroforestry.org/ (last accessed on 12/November/2021).

Geogdzhayev, I.V., Marshak, A., 2018. Calibration of the DSCOVR EPIC visible and NIR channels using MODIS Terra and Aqua data and EPIC lunar observations. Atmos. Measure Tech. 11, 359–368.

Gitelson, A.A., 2004. Wide dynamic range vegetation index for remote quantification of biophysical characteristics of vegetation. J. Plant Physiol. 161, 165–173.

Gitelson, A.A., 2013. Remote estimation of crop fractional vegetation cover: the use of noise equivalent as an indicator of performance of vegetation indices. Int. J. Remote Sens. 34, 6054–6066.

Gitelson, A.A., Kaufman, Y.J., Stark, R., Rundquist, D., 2002. Novel algorithms for remote estimation of vegetation fraction. Remote Sens. Environ. 80, 76–87.

Goel, N.S., Strebel, D.E., 1984. Simple Beta distribution representation of leaf orientation in vegetation canopies. Agron. J. 76, 800–802.

Gorkavyi, N., Carn, S., DeLand, M., Knyazikhin, Y., Krotkov, N., Marshak, A., Myneni, R., Vasilkov, A., 2021. Earth imaging from the surface of the moon with a DSCOVR/EPIC-type camera. Front. Remote Sens. 2, 1–11.

Guan, K., Wood, E.F., Caylor, K.K., 2012. Multi-sensor derivation of regional vegetation fractional cover in Africa. Remote Sens. Environ. 124, 653–665.

Gutman, G., Ignatov, A., 1998. The derivation of the green vegetation fraction from NOAA/AVHRR data for use in numerical weather prediction models. Int. J. Remote Sens. 19, 1533–1543.

Hansen, M.C., Potapov, P.V., Moore, R., Hancher, M., Turubanova, S.A., Tyukavina, A., Thau, D., Stehman, S.V., Goetz, S.J., Loveland, T.R., Kommareddy, A., Egorov, A., Chini, L., Justice, C.O., Townshend, J.R.G., 2013. High-resolution global maps of 21st-century forest cover change. Science 342, 850–853.

Hapke, B., DiMucci, D., Nelson, R., Smythe, W., 1996. The cause of the hot spot in vegetation canopies and soils: shadow-hiding versus coherent backscatter. Remote Sens. Environ. 58, 63–68.

He, L., Chen, J.M., Pisek, J., Schaaf, C.B., Strahler, A.H., 2012. Global clumping index map derived from the MODIS BRDF product. Remote Sens. Environ. 119, 118–130.

Herman, J., Huang, L., McPeters, R., Ziemke, J., Cede, A., Blank, K., 2018. Synoptic ozone, cloud reflectivity, and erythemal irradiance from sunrise to sunset for the whole earth as viewed by the DSCOVR spacecraft from the Earth–Sun Lagrange 1 Orbit. Atmos. Measure Tech. 11, 177–194.

Hilker, T., Galvão, L.S., Aragão, L.E.O.C., de Moura, Y.M., do Amaral, C.H., Lyapustin, A. I., Wu, J., Albert, L.P., Ferreira, M.J., Anderson, L.O., dos Santos, V.A.H.F., Prohaska, N., Tribuzy, E., Barbosa Ceron, J.V., Saleska, S.R., Wang, Y., de Carvalho Gonçalves, J.F., de Oliveira Junior, R.C., Cardoso Rodrigues, J.V.F., Garcia, M.N., 2017. Vegetation chlorophyll estimates in the Amazon from multi-angle MODIS observations and canopy reflectance model. Int. J. Appl. Earth Obs. Geoinf. 58, 278–287.

Hirano, Y., Yasuoka, Y., Ichinose, T., 2004. Urban climate simulation by incorporating satellite-derived vegetation cover distribution into a mesoscale meteorological model. Theor. Appl. Climatol. 79, 175–184.

Houborg, R., McCabe, M.F., 2018. Daily retrieval of NDVI and LAI at 3 m resolution via the fusion of Cubesat, Landsat, and MODIS data. Remote Sens. 10, 890.

Houborg, R., Soegaard, H., Boegh, E., 2007. Combining vegetation index and model inversion methods for the extraction of key vegetation biophysical parameters using Terra and Aqua MODIS reflectance data. Remote Sens. Environ. 106, 39–58.

Huete, A., 1988. A soil-adjusted vegetation index (SAVI). Remote Sens. Environ. 25, 295–309.

Idso, S., Jackson, R., Reginato, R., Kimball, B., Nakayama, F., 1975. The dependence of bare soil albedo on soil water content. J. Appl. Meteorol. Climatol. 14, 109–113.

Jeong, S.-J., Ho, C.-H., Gim, H.-J., Brown, M.E., 2011. Phenology shifts at start vs. end of growing season in temperate vegetation over the northern hemisphere for the period 1982–2008. Glob. Chang. Biol. 17, 2385–2399.

Jia, K., Liang, S., Liu, S., Li, Y., Xiao, Z., Yao, Y., Jiang, B., Zhao, X., Wang, X., Xu, S., Cui, J., 2015. Global land surface fractional vegetation cover estimation using general regression neural networks from MODIS surface reflectance. IEEE Trans. Geosci. Remote Sens. 53, 4787–4796.

Jiang, Z., Huete, A.R., Didan, K., Miura, T., 2008. Development of a two-band enhanced vegetation index without a blue band. Remote Sens. Environ. 112, 3833–3845.

Jiang, H., Wang, S., Cao, X., Yang, C., Zhang, Z., Wang, X., 2019. A shadow- eliminated vegetation index (SEVI) for removal of self and cast shadow effects on vegetation in rugged terrains. Int. J. Digit Earth 12, 1013–1029.

Jiapaer, G., Chen, X., Bao, A., 2011. A comparison of methods for estimating fractional vegetation cover in arid regions. Agric. For. Meteorol. 151, 1698–1710.

Jupp, D.L.B., Strahler, A.H., 1991. A hotspot model for leaf canopies. Remote Sens. Environ. 38, 193–210.

Kucharik, C.J., Norman, J.M., Gower, S.T., 1999. Characterization of radiation regimes in nonrandom forest canopies: theory, measurements, and a simplified modeling approach. Tree Physiol. 19, 695–706.

Kuusk, A., 1985. The hot spot effect on a uniform vegetative cover. Sov. J. Remote. Sens. 3, 645–658.

Kuusk, A., 1991. The hot spot effect in plant canopy reflectance. In: Myneni, R., Ross, J. (Eds.), Photon-Vegetation Interactions. Springer, Berlin Heidelberg, pp. 139–159.

Li, X., Strahler, A.H., 1985. Geometric-optical modeling of a conifer forest canopy. IEEE Trans. Geosci. Remote Sens. 23, 705–721.

Li, X., Strahler, A.H., 1992. Geometric-optical bidirectional reflectance modeling of the discrete crown vegetation canopy: effect of crown shape and mutual shadowing. IEEE Trans. Geosci. Remote Sens. 30, 276–292.

Liu, L., Zhang, X., 2020. Effects of temperature variability and extremes on spring phenology across the contiguous United States from 1982 to 2016. Sci. Rep. 10, 17952.

Lu, H., Raupach, M.R., McVicar, T.R., Barrett, D.J., 2003. Decomposition of vegetation cover into Woody and Herbaceous components using AVHRR NDVI time series. Remote Sens. Environ. 86, 1–18.

Lyapustin, A., Wang, Y., Go, S., Choi, M., Korkin, S., Huang, D., Knyazikhin, Y., Blank, K., Marshak, A., 2021. Atmospheric correction of DSCOVR EPIC: version 2 MAIAC algorithm. Front. Remote Sens. 2, 1–10.

Marshak, A., 2020. Summary of the fifth DSCOVR science team meeting. In: In, the Earth Observer. NASA Goddard Space Flight Center: Science Support Office, pp. 29–34. https://eospso.gsfc.nasa.gov/sites/default/files/eo_pdfs/Jan_Feb_2020_color_508_final.pdf (accessed on 12/November/2021).

Marshak, A., Ward, A., 2018. Summary of DSCOVR EPIC and NISTAR science team meeting. In: The Earth Observer. NASA Goddard Space Flight Center: Science Support Office, pp. 16–22. https://eospso.gsfc.nasa.gov/sites/default/files/eo_pdfs/Nov_Dec_2018_color508_0.pdf (accessed on 12/November/2021).

Marshak, A., Herman, J., Adam, S., Karin, B., Carn, S., Cede, A., Geogdzhayev, I., Huang, D., Huang, L.-K., Knyazikhin, Y., 2018. Earth observations from DSCOVR EPIC instrument. Bull. Am. Meteorol. Soc. 99, 1829–1850.

McVicar, T.R., Jupp, D.L.B., Reece, P.H., Williams, N.A., 1996a. Relating Landsat TM vegetation indices to in situ leaf area index measurements. In: Division of Water Resources, Technical Memorandum. CSIRO, Canberra, Australia, p. 80.

McVicar, T.R., Jupp, D.L.B., Williams, N.A., 1996b. Relating AVHRR vegetation indices to Landsat TM leaf area index estimates. In: Division of Water Resources, Technical Memorandum. CSIRO, Canberra, Australia, p. 29.

Montandon, L.M., Small, E.E., 2008. The impact of soil reflectance on the quantification of the green vegetation fraction from NDVI. Remote Sens. Environ. 112, 1835–1845.

Morcillo-Pallarés, P., Rivera-Caicedo, J.P., Belda, S., De Grave, C., Burriel, H., Moreno, J., Verrelst, J., 2019. Quantifying the robustness of vegetation indices through global sensitivity analysis of homogeneous and forest leaf-canopy radiative transfer models. Remote Sens. 11, 2418–2441.

Mu, X., Huang, S., Ren, H., Yan, G., Song, W., Ruan, G., 2015. Validating GEOV1 fractional vegetation cover derived from coarse-resolution remote sensing images over croplands. IEEE J. Select. Top. Appl. Earth Observ. Remote Sens. 8, 439–446.

Mu, X., Song, W., Gao, Z., McVicar, T.R., Donohue, R.J., Yan, G., 2018. Fractional vegetation cover estimation by using multi-angle vegetation index. Remote Sens. Environ. 216, 44–56.

Mu, X., Zhao, T., Ruan, G., Song, J., Wang, J., Yan, G., McVicar, T.R., Yan, K., Gao, Z., Liu, Y., 2021. High spatial resolution and high temporal frequency (30-m/15-day) fractional vegetation cover estimation over China using multiple remote sensing datasets: method development and validation. J. Meteorol. Res. 34, 1–21.

Myneni, R.B., Kanemasu, E.T., 1988. The hot spot of vegetation canopies. J. Quant. Spectrosc. Radiat. Transf. 40, 165–168.

Myneni, R., Knyazikhin, Y., Park, T., 2015. MOD15A2H MODIS/Terra Leaf Area Index/FPAR 8-Day L4 Global 500 m Sin Grid V006. NASA EOSDIS Land Processes DAAC. https://lpdaac.usgs.gov/products/mod15a2hv006/ (last accessed on 12/November/2021).

Ni, X., Knyazikhin, Y., Sun, Y., She, X., Guo, W., Panferov, O., Myneni, R.B., 2021. Vegetation angular signatures of equatorial forests from DSCOVR EPIC and Terra MISR observations. Front. Remote Sens. 2, 1–14.

Nilson, T., 1971. A theoretical analysis of the frequency of gaps in plant stands. Agric. Meteorol. 8, 25–38.

Nilson, T., 1991. Approximate analytical methods for calculating the reflection functions of leaf canopies in remote sensing applications. In: Myneni, R., Ross, J. (Eds.), Photon-Vegetation Interactions. Springer, Berlin Heidelberg, pp. 161–190.

Nouvellon, Y., Bégué, A., Moran, M.S., Seen, D.L., Rambal, S., Luquet, D., Chehbouni, G., Inoue, Y., 2000. PAR extinction in shortgrass ecosystems: effects of clumping, sky conditions and soil albedo. Agricult. For. Meteorol. 105, 21–41.

Ormsby, J.P., Choudhury, B.J., Owe, M., 1987. Vegetation spatial variability and its effect on vegetation indices. Int. J. Remote Sens. 8, 1301–1306.

Pal, J.S., Giorgi, F., Bi, X., Elguindi, N., Solmon, F., Gao, X., Rauscher, S.A., Francisco, R., Zakey, A., Winter, J., 2007. Regional climate modeling for the developing world: the ICTP RegCM3 and RegCNET. Bull. Am. Meteorol. Soc. 88, 1395–1410.

Pan, G., Xu, Y., Ma, J., 2021. The potential of CO_2 satellite monitoring for climate governance: a review. J. Environ. Manag. 277, 111423.

Peng, J., Fan, W., Wang, L., Xu, X., Li, J., Zhang, B., Tian, D., 2018. Modeling the directional clumping index of crop and forest. Remote Sens. 10, 1576–1598.

Pérez, L., Fuster, B., Camacho, F., 2019. Scientific Quality Evaluation LAI, FAPAR, FCOVER Collection 1km Version 1 & Version 2. In J. Sánchez-Zapero (Ed.), Copernicus Global Land Operations "Vegetation and Energy" " Cglops-1": Copernicus. https://land.copernicus.eu/global/products/fcover (last accessed on 12/November/2021).

Pisek, J., Arndt, S.K., Erb, A., Pendall, E., Schaaf, C., Wardlaw, T.J., Woodgate, W., Knyazikhin, Y., 2021. Exploring the potential of DSCOVR EPIC data to retrieve clumping index in Australian terrestrial ecosystem research network observing sites. Front. Remote Sens. 2, 1–9.

Qi, J., Xie, D., Yin, T., Yan, G., Gastellu-Etchegorry, J.-P., Li, L., Zhang, W., Mu, X., Norford, L.K., 2019. LESS: large-scale remote sensing data and image simulation framework over heterogeneous 3D scenes. Remote Sens. Environ. 221, 695–706.

Qin, W., Xiang, Y., 1994. On the hotspot effect of leaf canopies: modeling study and influence of leaf shape. Remote Sens. Environ. 50, 95–106.

Qin, W., Goel, N.S., Wang, B., 1996. The hotspot effect in heterogeneous vegetation canopies and performances of various hotspot models. Remote Sens. Rev. 14, 283–332.

Richardson, A.D., Keenan, T.F., Migliavacca, M., Ryu, Y., Sonnentag, O., Toomey, M., 2013. Climate change, phenology, and phenological control of vegetation feedbacks to the climate system. Agric. For. Meteorol. 169, 156–173.

Rocha, A.V., Shaver, G.R., 2009. Advantages of a two band EVI calculated from solar and photosynthetically active radiation fluxes. Agric. For. Meteorol. 149, 1560–1563.

Roujean, J.-L., Leroy, M., Deschamps, P.-Y., 1992. A bidirectional reflectance model of the earth's surface for the correction of remote sensing data. J. Geophys. Res.-Atmos. 97, 20455–20468.

Sellers, P.J., Tucker, C.J., Collatz, G.J., Los, S.O., Justice, C.O., Dazlich, D.A., Randall, D. A., 1996. A revised land surface parameterization (SiB2) for atmospheric GCMS. Part II: the generation of global fields of terrestrial biophysical parameters from satellite data. J. Clim. 9, 706–737.

Sitch, S., Smith, B., Prentice, I.C., Arneth, A., Bondeau, A., Cramer, W., Kaplan, J.O., Levis, S., Lucht, W., Sykes, M.T., 2003. Evaluation of ecosystem dynamics, plant geography and terrestrial carbon cycling in the LPJ dynamic global vegetation model. Glob. Chang. Biol. 9, 161–185.

Skamarock, W., Klemp, J., Dudhia, J., Gill, D., Barker, D., Duda, M., Huang, X.-Y., Wang, W., Powers, J., 2008. A Description of the Advanced Research WRF Version 3. NCAR Technical Note, NCAR/Tn-475+Str. National Center for Atmospheric Research, Boulder, Colorado, USA. https://www.mmm.ucar.edu/wrf-release-information (last accessed on 12/November/2021).

Sobrino, J.A., Julien, Y., Soria, G., 2013. Phenology estimation from Meteosat second generation data. IEEE J. Select. Top. Appl. Earth Observ. Remote Sens. 6, 1653–1659.

Song, W., Mu, X., Yan, G., Huang, S., 2015. Extracting the Green fractional vegetation cover from digital images using a shadow-resistant algorithm (SHAR-LABFVC). Remote Sens. 7, 10425–10443.

Song, W., Mu, X., Ruan, G., Gao, Z., Li, L., Yan, G., 2017. Estimating fractional vegetation cover and the vegetation index of bare soil and highly dense vegetation with a physically based method. Int. J. Appl. Earth Obs. Geoinf. 58, 168–176.

Song, W., Knyazikhin, Y., Wen, G., Marshak, A., Möttus, M., Yan, K., Yang, B., Xu, B., Park, T., Chen, C., Zeng, Y., Yan, G., Mu, X., Myneni, R., 2018. Implications of whole-disc DSCOVR EPIC spectral observations for estimating earth's spectral reflectivity based on low-earth-orbiting and geostationary observations. Remote Sens. 10, 1594–1617.

Strahler, A.H., Jupp, D.L.B., 1990. Modeling bidirectional reflectance of forests and woodlands using Boolean models and geometric optics. Remote Sens. Environ. 34, 153–166.

Sun, Y., Knyazikhin, Y., She, X., Chen, C., Ren, H., Myneni, R.B., 2021. Seasonal and long-term variations in leaf area of Congolese rainforest. Remote Sens. Environ. https://doi.org/10.1016/j.rse.2021.112762) (Accept; doi: 10.1016/j. rse.2021.112762).

Vargas, M., Jiang, Z., Ju, J., Csiszar, I., 2013. EVI Based Green Vegetation Fraction Derived from Suomi NPP-VIIRS. Preprints. Ninth Symp. Future Operational Env. Sat. Systems. https://viirsland.gsfc.nasa.gov/Products/NOAA/GVF.html (last accessed on 12/November/2021).

Verger, A., Baret, F., Weiss, M., 2014a. Near real-time vegetation monitoring at global scale. IEEE J. Select. Top. Appl. Earth Observ. Remote Sens. 7, 3473–3481.

Verger, A., Baret, F., Weiss, M., Smets, B., Camacho, F., Lacaze, R., 2014b. GEOV2/VGT: Near real time estimation of LAI FAPAR and cover fraction variables from vegetation data within Copernicus global land service. In: The 4th International Symposium on Recent Advances in Quantitative Remote Sensing, 2014, Valence, Spain. https://ipl.uv.es/raqrs5/?q=content/home-raqrsiv (last accessed on 12/November/2021).

Vermote, E., Justice, C., Claverie, M., Franch, B., 2016. Preliminary analysis of the performance of the Landsat 8/OLI land surface reflectance product. Remote Sens. Environ. 185, 46–56.

Verstraete, M.M., Pinty, B., Dickinson, R.E., 1990. A physical model of the bidirectional reflectance of vegetation canopies: 1. Theory. J. Geophys. Res.-Atmos. 95, 11755–11765.

Wang, W.M., Li, Z.L., Su, H.B., 2007. Comparison of leaf angle distribution functions: effects on extinction coefficient and fraction of sunlit foliage. Agric. For. Meteorol. 143, 106–122.

Wanner, W., Li, X., Strahler, A.H., 1995. On the derivation of kernels for kernel-driven models of bidirectional reflectance. J. Geophys. Res.-Atmos. 100, 21077–21089.

Weiss, M., Baret, F., Smith, G.J., Jonckheere, I., Coppin, P., 2004. Review of methods for in situ leaf area index (LAI) determination. Agric. For. Meteorol. 121, 37–53.

Wen, G., Marshak, A., Song, W., Knyazikhin, Y., Möttus, M., Wu, D., 2019. A relationship between blue and near-IR global spectral reflectance and the response of global average reflectance to change in cloud cover observed from EPIC. Earth Space Sci. 6, 1416–1429.

Widlowski, J.-L., Pinty, B., Lavergne, T., Verstraete, M.M., Gobron, N., 2006. Horizontal radiation transport in 3-D forest canopies at multiple spatial resolutions: simulated impact on canopy absorption. Remote Sens. Environ. 103, 379–397.

Widlowski, J.-L., Lavergne, T., Pinty, B., Gobron, N., Verstraete, M.M., 2008. Towards a high spatial resolution limit for pixel-based interpretations of optical remote sensing data. Adv. Space Res. 41, 1724–1732.

Widlowski, J.-L., Pinty, B., Lopatka, M., Atzberger, C., Buzica, D., Chelle, M., Disney, M., Gastellu-Etchegorry, J.-P., Gerboles, M., Gobron, N., Grau, E., Huang, H., Kallel, A., Kobayashi, H., Lewis, P.E., Qin, W., Schlerf, M., Stuckens, J., Xie, D., 2013. The fourth radiation transfer model intercomparison (RAMI-IV): proficiency testing of canopy reflectance models with ISO-13528. J. Geophys. Res.-Atmos. 118, 6869–6890.

Widlowski, J.-L., Mio, C., Disney, M., Adams, J., Andredakis, I., Atzberger, C., Brennan, J., Busetto, L., Chelle, M., Ceccherini, G., Colombo, R., Côté, J.-F., Eenmäe, A., Essery, R., Gastellu-Etchegorry, J.-P., Gobron, N., Grau, E., Haverd, V., Homolová, L., Huang, H., Hunt, L., Kobayashi, H., Koetz, B., Kuusk, A., Kuusk, J., Lang, M., Lewis, P.E., Lovell, J.L., Malenovský, Z., Meroni, M., Morsdorf, F., Möttus, M., Ni-Meister, W., Pinty, B., Rautiainen, M., Schlerf, M., Somers, B., Stuckens, J., Verstraete, M.M., Yang, W., Zhao, F., Zenone, T., 2015. The fourth phase of the radiative transfer model intercomparison (RAMI) exercise: actual canopy scenarios and conformity testing. Remote Sens. Environ. 169, 418–437.

Wilson, A.M., Jetz, W., 2016. Remotely sensed high-resolution global cloud dynamics for predicting ecosystem and biodiversity distributions. PLoS Biol. 14, e1002415.

Woodcock, C.E., Collins, J.B., Jakabhazy, V.D., Xiaowen, L., Macomber, S.A., Yecheng, W., 1997. Inversion of the Li-Strahler canopy reflectance model for mapping forest structure. IEEE Trans. Geosci. Remote Sens. 35, 405–414.

Xiao, X., Hollinger, D., Aber, J., Goltz, M., Davidson, E.A., Zhang, Q., Moore III, B., 2004. Satellite-based modeling of gross primary production in an Evergreen Needleleaf Forest. Remote Sens. Environ. 89, 519–534.

Xiao, Z., Wang, T., Liang, S., Sun, R., 2016. Estimating the fractional vegetation cover from GLASS leaf area index product. Remote Sens. 8, 337–356.

Yan, D., Zhang, X., Yu, Y., Guo, W., 2016a. A comparison of tropical rainforest phenology retrieved from geostationary (SEVIRI) and polar-orbiting (MODIS) sensors across the Congo Basin. IEEE Trans. Geosci. Remote Sens. 54, 4867–4881.

Yan, K., Park, T., Yan, G., Liu, Z., Yang, B., Chen, C., Nemani, R.R., Knyazikhin, Y., Myneni, R.B., 2016b. Evaluation of MODIS LAI/FPAR product collection 6. Part 2: validation and Intercomparison. Remote Sens. 8, 460–486.

Yan, K., Gao, S., Chi, H., Qi, J., Song, W., Tong, Y., Mu, X., Yan, G., 2021. Evaluation of the vegetation-index-based dimidiate pixel model for fractional vegetation cover estimation. IEEE Trans. Geosci. Remote Sens. 1–14.

Yang, B., Knyazikhin, Y., Möttus, M., Rautiainen, M., Stenberg, P., Yan, L., Chen, C., Yan, K., Choi, S., Park, T., 2017. Estimation of leaf area index and its sunlit portion from DSCOVR EPIC data: theoretical basis. Remote Sens. Environ. 198, 69–84.

Yu, F., Wu, X., 2016. Radiometric inter-calibration between Himawari-8 AHI and S-NPP VIIRS for the solar reflective bands. Remote Sens. 8, 1–16.

Zeng, X., Dickinson, R.E., Walker, A., Shaikh, M., DeFries, R.S., Qi, J., 2000. Derivation and evaluation of global 1-km fractional vegetation cover data for land modeling. J. Appl. Meteorol. 39, 826–839.

Zhang, X., Tarpley, D., Sullivan, J.T., 2007. Diverse responses of vegetation phenology to a warming climate. Geophys. Res. Lett. 34, L19405.

Zhang, L., Sun, X., Wu, T., Zhang, H., 2015. An analysis of shadow effects on spectral vegetation indexes using a ground-based imaging spectrometer. IEEE Geosci. Remote Sens. Lett. 12, 2188–2192.

Zhang, C., Ma, L., Chen, J., Rao, Y., Zhou, Y., Chen, X., 2019. Assessing the impact of endmember variability on linear spectral mixture analysis (LSMA): A theoretical and simulation analysis. Remote Sens. Environ. 235, 111471.